



ELSEVIER

Contents lists available at ScienceDirect

Journal of Building Engineering

journal homepage: www.elsevier.com/locate/job

Experimental and theoretical analyses of the progressive collapse resistance of NSM strengthening RC frames after the failure of a corner column

Weihong Qin^{a,b}, Zhuo Xi^{a,b,*}, Xinyu Liu^{a,b}, Peng Feng^c, Xin Ou^a, Jianxiang Yang^c

^a The Key Laboratory of Concrete and Prestressed Concrete Structures of Ministry of Education, Southeast University, Nanjing, 211189, China

^b National Prestress Engineering Research Center, Southeast University, Nanjing, 211189, China

^c Department of Civil Engineering, Tsinghua University, Beijing, 100084, China

ARTICLE INFO

Keywords:

Reinforced concrete frame
Progressive collapse
Corner-column removal
Principle of virtual work
Yield line method

ABSTRACT

When exposed to accidental loads, reinforced concrete (RC) frames are vulnerable to progressive collapse after the failure of a corner column, so necessary strengthening schemes should be employed for the frame. By strengthening the slab with near-surface-mounted (NSM) glass fiber-reinforced polymer (GFRP) bars and engineered cementitious composites (ECC) layer, this study experimentally revealed the effect of the strengthening method on the progressive collapse behavior of beam-slab systems after the removal of a corner column. Then, on the basis of experimental results, a theoretical analysis method of the peak capacity for the beam-slab system is proposed according to the principle of virtual work and the yield-line theory. The derived formula can accurately predict the progressive collapse resistance of the RC beam-slab system after the failure of a corner column and quantitatively evaluate the contribution of floor slabs to the structural capacity. The validity of the method is also proven by the application to the structural capacity of a flat-slab system and a beam-column system. Finally, according to the theoretical formula, the influence of several parameters on the structural capacity is investigated, such as the earthquake fortification intensity of the frame, the over-strength factors, the column spacing, and the depth-to-span ratio of the beam. The research results demonstrate that after considering the L-beam action, the capacities of the test specimens can be improved by 52%–65%. The capacity of the flat-slab system is the lowest among the above three structural systems. The structural progressive collapse resistance can be effectively improved through enhancing the constraint stiffness of the corner beam-column joint and utilizing building materials with high plastic development ability.

1. Introduction

The disproportionate collapse of Ronan Point Apartments in London that occurred in 1968 lifted the curtain of the study on the progressive collapse behavior of structures. The collapse of Murrah Federal Building in Oklahoma City occurred in 1995, and the collapse of World Trade Center Building in New York City appeared in 2001, leading to progressive collapse resistance to a popular research topic around the world. To ensure the progressive collapse resistance of building structures, several structural design codes

* Corresponding author. The Key Laboratory of Concrete and Prestressed Concrete Structures of Ministry of Education, Southeast University, Nanjing, 211189, China.

E-mail address: xizhuoxian@seu.edu.cn (Z. Xi).

<https://doi.org/10.1016/j.job.2021.103805>

Received 28 September 2021; Received in revised form 23 November 2021; Accepted 30 November 2021

Available online 2 December 2021

2352-7102/© 2021 Published by Elsevier Ltd.

[1–3] and special guidelines [4,5] have been proposed over the past years. The above codes and guidelines mainly involve four design methods, i.e., conceptual design method, tie force method, alternate load path (ALP) method, and enhanced local resistance method.

The ALP method [4] employs three analysis procedures: linear static, nonlinear static, and nonlinear dynamic, among which the nonlinear dynamic procedure provides the most direct simulation of the actual structural behavior and hence is the most accurate procedure. However, due to the complicated procedures in nonlinear dynamic experiments, the nonlinear static procedure is frequently used for the quantitative analysis of structural collapse resistance. Based on the ALP method, studies on the progressive collapse behavior of reinforced concrete (RC) frame structures mainly focus on the removal scenario of a middle column, an edge column or a corner column.

According to experimental results and numerical simulations, research papers [6–12] confirmed that after the removal of a middle column or an edge column, the frame developed three different mechanisms, i.e., flexural action, compressive arch action, and catenary action. Furthermore, researchers [10,13–15] conducted theoretical analysis and proposed calculation formulas of progressive collapse resistance at each mechanism stage, which explained the principle of the mechanism actions on the improvement of structural collapse resistance.

Nevertheless, Qian and Li [16,17] reported that after the removal of a corner column, compressive arch action and catenary action cannot be effectively mobilized in a beam-column system due to the relatively weak constraint on edge beams; thus, the structural capacity is solely contributed by flexural action. Therefore, the progressive collapse resistance of a frame subjected to the failure of a corner column is the lowest among all column-removal scenarios. To mitigate the vulnerability of the progressive collapse of the beam-column system, the arrangement of the slab is essential. Due to the contribution of slabs, the static [16] and dynamic [18] capacity of the beam-slab system can be significantly improved compared with those of the beam-column system after the removal of a corner column. The above improvement of the structural capacity mainly benefits from the L-beam action. Papers [10,11] indicated that catenary action developed in RC beam-slab systems at large deformations and that the slabs were beneficial for resisting progressive collapse of frames. In addition, to reduce the likelihood of structural progressive collapse under a corner column-removal scenario, necessary strengthening schemes have been applied. Qian et al. [19] and Feng et al. [20] implemented progressive collapse experiments of strengthening schemes aimed at slabs in flat-slab systems and beam-slab systems after the loss of a corner column, respectively. The strengthening methods contain externally bonded (EBR) and near-surface-mounted (NSM) FRP materials. Test results from the above studies proved that the strengthening schemes with FRP materials were effective in improving the structural progressive collapse resistance. Also, Kang et al. [21] experimentally investigated the progressive collapse behavior of precast concrete beam-column systems strengthened with engineered cementitious composites (ECC) under a middle column-removal scenario, and test results found that the utilization of ECC on beams obviously changed the crack patterns and failure modes of specimens.

This study experimentally reported and compared the progressive collapse behavior of beam-slab assemblages strengthened with near-surface-mounted GFRP bars and ECC layer after the failure of a corner column. Then, on the basis of experimental results, the calculation method of peak capacity for the beam-slab system was proposed, and the potential of progressive collapse was evaluated in this paper. Furthermore, to prove the validity of the theoretical method, capacity comparisons between theoretical results and experimental results were conducted for different structural systems, and good agreements were found. According to the above theory, parametric analyses revealed the effects of the various structural factors on the progressive collapse behavior of frames under a corner column-removal scenario.

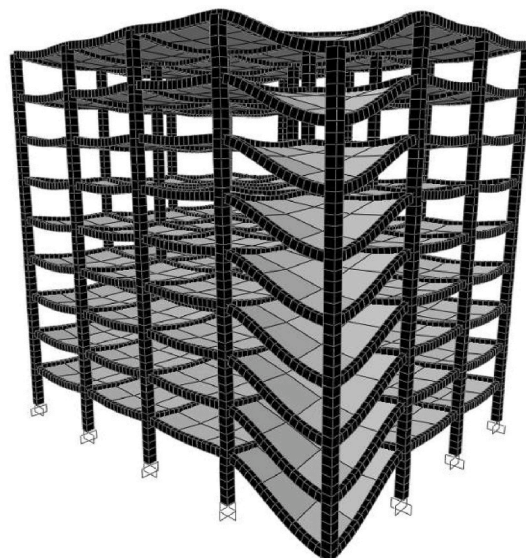


Fig. 1. Typical failure mode of a frame structure after the failure of a corner column.

2. Experimental program

2.1. The prototype frame and specimen design

Frame structures are vulnerable to progressive collapse after the failure of a corner column because of the lack of sufficient constraints from surrounding components, and the typical failure mode of a frame structure is illustrated in Fig. 1. Progressive collapse accidents caused by the failure of corner columns indicate that the structural capacity is insufficient to resist the gravity load applied on the frame and that the frame needs to be strengthened.

The prototype frame is a 6-story RC frame designed in accordance with the building codes [22,23]. The first story is 3.9 m in height, and the remaining stories are 3.6 m in height. The dead and live loads in the design are 5.5 kN/m^2 and 2.0 kN/m^2 , respectively. As shown in Fig. 2, the research element enclosed by the dashed lines consists of four columns (designated as column A, B, C and D), four beams (beam AB, BC, CD, and AD) with identical section dimensions and reinforcement details and slabs. The research element is scaled to 1/2 as the control specimen according to the principle of equal reinforcement ratio. The dimensions and reinforcement details of the control specimen are shown in Fig. 3. The yield strength and ultimate strength for HRB400-grade steel bar with a diameter of 12 mm were 427 MPa and 530 MPa, respectively, and the yield strength and ultimate strength for HPB300-grade steel bar with a diameter of 6 mm were 324 MPa and 525 MPa, respectively.

In addition to the control specimen US, the performance of two beam-slab subassemblages strengthened with near-surface-mounted GFRP bars (specimen NSM-series) in resisting progressive collapse was also investigated. For specimen NSM-series, GFRP bars with a diameter (d) of 6 mm were embedded in the grooves of the slab top at an interval of 200 mm and 300 mm for NSM1 and NSM2, respectively. In addition, an engineered cementitious composite (ECC) layer with a thickness of 15 mm covered the slab top face of specimen NSM2 to study the effect of the good ductility of ECC on the collapse resistance of frame structures. The strengthening details of the above specimens are listed in Table 1, and the material properties of ECC are given in Table 2.

Also in Table 1, the equivalent strengthening quantity is introduced to quantify the amount of GFRP bars used in specimen NSM-series. The equivalent strengthening quantity of specimen NSM1 and NSM2 is 2.0 and 1.33 times $f_y A_{sbt}$, respectively, in which f_y is the yield strength of distributed reinforcements of the slab, and A_{sbt} is the total area of x-direction or y-direction bottom distributed reinforcements of the slab. Therefore, the effect of equivalent strengthening quantity of GFRP bars on the collapse resistance of beam-slab subassemblages after the failure of a corner column can be investigated.

2.2. Test setup

The quasi-static loading scheme was adopted to apply the vertical load on the specimens, and the test setup is indicated in Fig. 4. In Fig. 4(a), stub B, C and D are separately fixed on their concrete piers, regarded as fixed supports, while stub A is free for loading, simulating the failure of a corner column. Moreover, a certain number of steel assemblies with a weight of 10.23 kN were placed on each extended area of scaled specimens to simulate the influence of negative bending moments provided by surrounding slabs on the structural behavior of corner region ABCD. In Fig. 4(b), to permit stub A to rotate freely around the axis parallel to the diagonal BD, a load transfer head was placed on the top of stub A.

2.3. Experimental results

2.3.1. Load responses of specimens

The load-displacement curves of all specimens are illustrated in Fig. 5. For the beam-slab subassemblages, the failure process was initiated by the cracking of the slab top and the reinforcements yielding at fixed end sections of edge beams. When displacements reached 50 mm, 50 mm, and 55 mm, the measured strains of top steel bars at the fixed beam end sections reached the yield strain ($2135 \mu\epsilon$), thus specimen US, NSM1, and NSM2 attained the yield loads of 35.0 kN, 45.0 kN, and 41.8 kN, respectively. Following that, plastic hinges formed at end B of beam AB and at end D of beam AD, with concrete crushing there. Compared with those of US, the initial stiffness of specimen NSM-series was enhanced, and the yield load was improved by 28.6% and 19.4% for NSM1 and NSM2, respectively.

With the increase of displacement, the loads of specimens continued to rapidly rise. At displacements of 85 mm, 81 mm, and 105

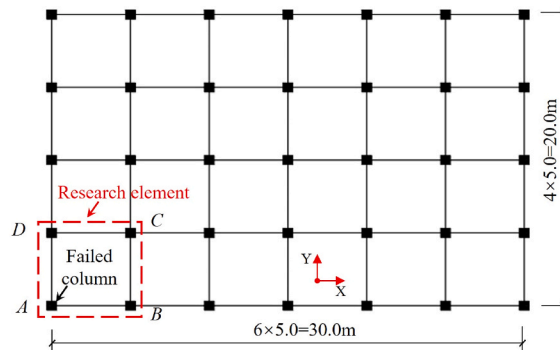


Fig. 2. Plan view of prototype frame and the location of research element.

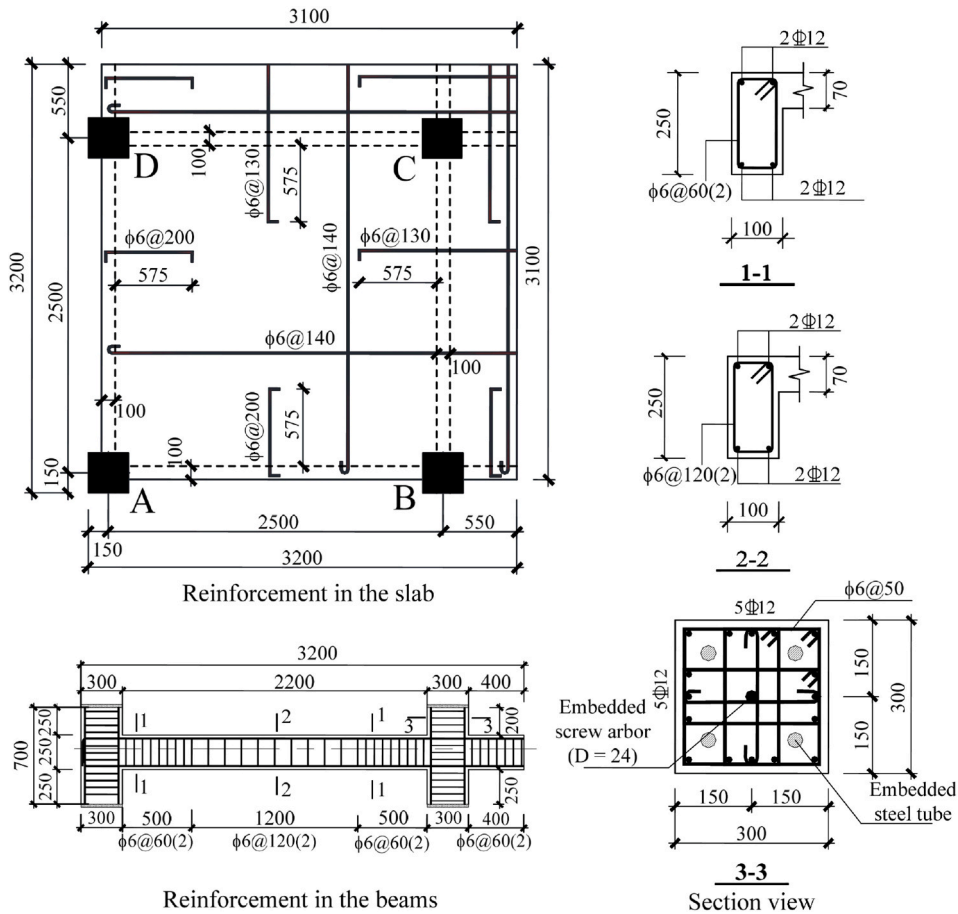


Fig. 3. Dimensions and reinforcement details of the control specimen (units: mm).

Table 1
Strengthening details of the specimens.

Specimen	Strengthening method	Strengthening detail (mm)	GFRP properties		Concrete strength f'_c (MPa)	Equivalent strengthening quantity
			E (GPa)	f_u (MPa)		
US	/	/	/	/	21.3	/
NSM1	Embedded GFRP bars	$d = 6, S = 200$	41.0	1113	20.6	$2.0 \cdot f_y \cdot A_{sbt}$
NSM2	Embedded GFRP bars and ECC layer	$d = 6, S = 300$ ECC layer thickness = 15	41.0	1113	18.7	$1.33 \cdot f_y \cdot A_{sbt}$

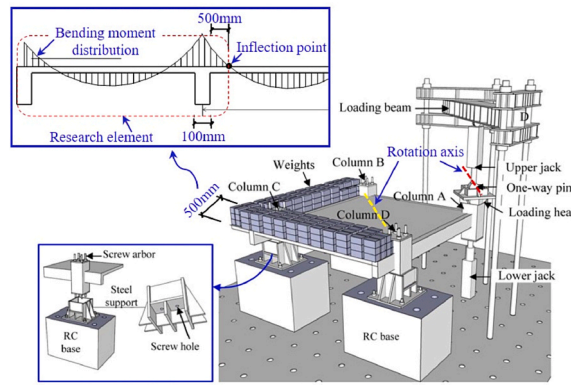
Note: d means the diameter of the GFRP bar; S means the spacing between each piece of GFRP bar; E and f_u indicate the elastic modulus and tensile strength of GFRP bars, respectively; f'_c represents the average cylinder compressive strength of the concrete.

Table 2
Material properties of ECC.

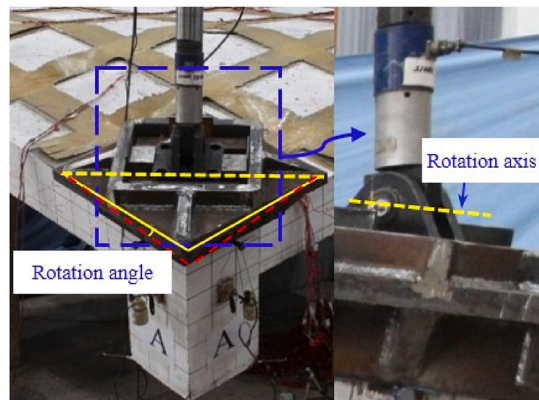
Compressive strength (MPa)	Ultimate compressive strain ($\mu\epsilon$)	Tensile strength (MPa)	Ultimate tensile strain ($\mu\epsilon$)
39.5	4000	5.8	18000

mm, specimen US, NSM1, and NSM2 reached the peak loads of 43.5 kN, 54.3 kN, and 53.0 kN, respectively. Compared with US, NSM1 and NSM2 could get a 24.8% and 21.8% enhancement of peak load, respectively, and the peak point was obviously delayed for specimen NSM2 due to ECC materials. Therefore, the above description demonstrated that the peak capacity of beam-slab assemblages can be dramatically improved by the NSM method under a corner column-removal scenario.

After the peak point, on further loading, severe concrete crushing and spalling, as well as the compressive buckling of steel bars, were presented at the beam ends, decreasing the loads of specimens. The experiment was stopped when the displacement reached 500



(a) Schematic view



(b) Load transfer head

Fig. 4. Test setup.

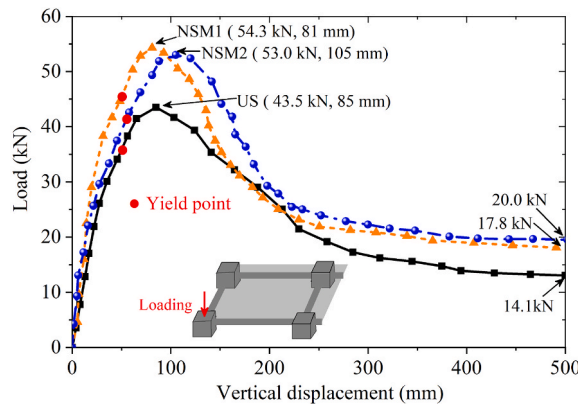


Fig. 5. Load-displacement curves of specimens.

mm, which was regarded as the final collapse failure of the specimen. The residual loads of NSM-series were significantly larger than that of US, and specimen NSM2, which was strengthened with both NSM GFRP bars and an ECC layer, had the largest residual load of 20.0 kN, as illustrated in Fig. 5. Therefore, it can be also concluded that the NSM method are beneficial to increase the residual load and reduce the progressive collapse risk of the frame. The final failure modes of all specimens are presented in Figs. 6–8.

2.3.2. Crack propagations of specimens

For the control specimen US, the cracks firstly appeared on the slab and beam around stub B. On further loading, the number of diagonal cracks increased rapidly on beam AB and AD under the combined action of bending, shear, and torsion. Also, severe diagonal cracks passed through the center of the slab after the load reached 25.0 kN. With the increase of vertical displacement, a main diagonal

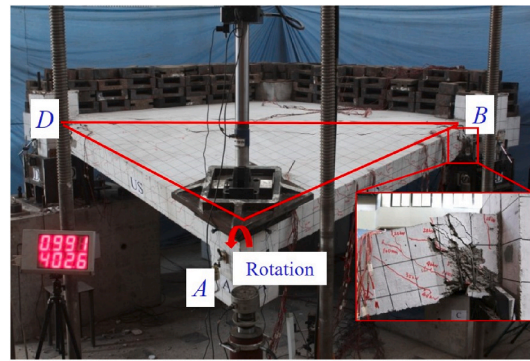


Fig. 6. Failure mode of specimen US.

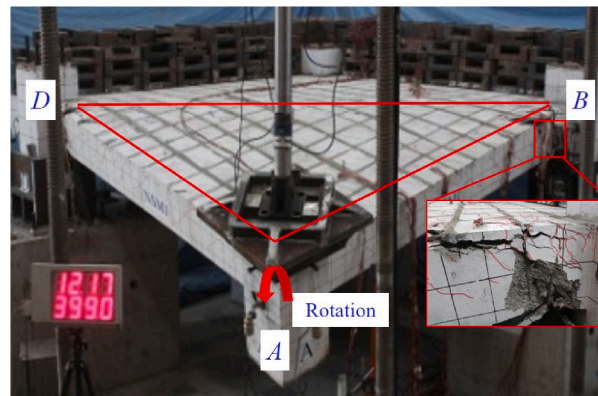


Fig. 7. Failure mode of specimen NSM1.

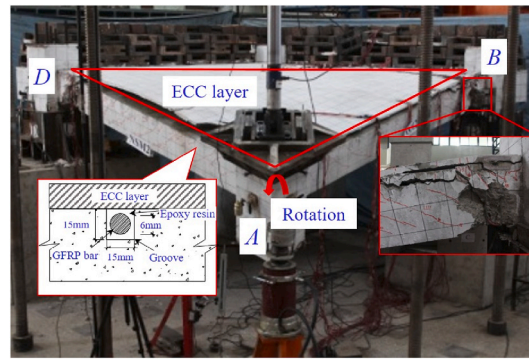
crack formed around slab yield line BD and the maximum width of the main crack approximated 15.0 mm. Finally, the whole triangle region ABD rotated and failed around slab yield line BD , and sparse cracks appeared in the slab top, which was regarded as collapse failure. The final crack distribution of the slab is shown in Fig. 9(a) for US.

For specimen NSM-series, the crack development of edge beams was similar to that of US, but the crack propagation of the slab was much different from that of US. For NSM1, the first cracks on the slab appeared near stub B and D , and then extended along the diagonal line BD . As loading continued, some cracks on the slab passed through the GFRP bars, resulting in the cracking of the adhesive layer in the grooves, which was effectively obstructed by the GFRP bars. The small cracks were densely distributed around the diagonal line BD . With the development of cracks, the debonding of GFRP bars gradually appeared on the slab top, but no main cracks were formed until the end of loading, as depicted in Fig. 9(b). For NSM2, the ECC layer can work compatibly with the slab at the initial loading stage, so closely-spaced hairline cracks propagated on the slab top. When the displacement reached 100 mm, the ECC layer began to debond from the triangle region ABD , and the cracks gradually penetrated the depth of ECC layer around stub A . At a displacement of 220 mm, the ECC layer was found to be completely debonded with the slab around stub A and finally fractured, as illustrated in Fig. 9(c).

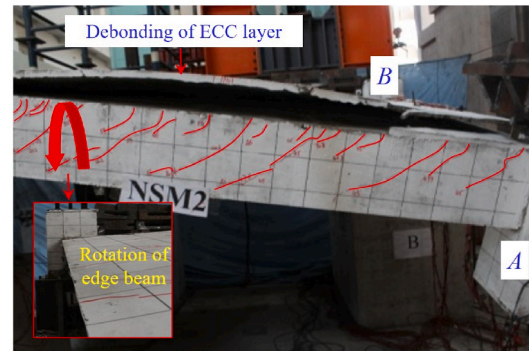
In general, for specimen NSM-series, dense cracks mainly occurred in the triangle region ABD without main cracks, and the crack width was obviously smaller than that of US. Therefore, the NSM method could help the cracks to distribute more uniformly on the slab top, and better utilize the strength of GFRP materials. In addition, due to the multi-cracking behavior of ECC materials, which can be attributed to the bridging effect of fibers, dense hairline cracks distributed on the slab top of specimen NSM2, indicating that the good ductility of ECC materials could improve the integrity of the whole specimen. Therefore, though the equivalent strengthening quantity of NSM2 is lower than that of NSM1 (Table 1), the peak capacities of specimen NSM-series are very close.

2.3.3. Strain responses of longitudinal reinforcements

The arrangement of strain gauges in the edge beam is illustrated in Fig. 10, in which strain gauges named by BT and BB measure the top and bottom longitudinal bar strains, respectively. Strain responses of steel bars at the plastic hinge zone (BT9 and BB9) and near the plastic hinge zone (BT7 and BB7) are chosen to be presented for all specimens. In Fig. 10(a), BT9 and BB9 were located at the flexural tensile zone and flexural compressive zone of the fixed beam end section, respectively, and both of them can attain the yield value ($2135 \mu\epsilon$) before a displacement of 100 mm. Besides, at BT9 and BB9, the strain growth rate of NSM1 was obviously larger than those of US and NSM2, which is consistent with the truth that NSM1 had the largest initial stiffness among all specimens (refer to Fig. 5). In Fig. 10(b), due to the relatively smaller flexural moments at the beam section of BT7 and BB7, the development of strains there was



(a) Elevation view



(b) Side view

Fig. 8. Failure mode of specimen NSM2.

slower than that at BT9 and BB9. For US and NSM1, the steel bars at BT7 yielded in tension from displacements of approximately 300 mm–350 mm, while BT7 of NSM2 reported no yielding until the end of loading, which can be attributed to the arrangement of an ECC layer on the beam top.

In Fig. 11, strain gauges named by ST and SB measure the top and bottom distributed bar strains of the slab, respectively, and the strain gauges results of ST1, ST7, ST10, SB14 are depicted. In Fig. 11(a), the strain at ST1 initially increased with the displacement, but after a displacement of 150 mm the strain tended to decrease gradually because the slab damage was concentrated along the diagonal line BD . In Fig. 11(b), ST7 was located at the diagonal BD , thus steel strains increased rapidly and soon reached the yield strain ($1543 \mu\epsilon$). Moreover, for US and NSM1, the strains at ST10 and SB14 were almost zero during the test, which indicates that the loading process has less impact on the triangle region BCD of the slab, so they were not displayed. Nevertheless, for NSM2, due to the good ductility of the ECC layer, the integrity of the whole specimen was enhanced (see the densely distributed hairline cracks on a large area of the slab top for NSM in Fig. 9(c)), and the strains at both ST10 and SB14 were in compression, as displayed in Fig. 11.

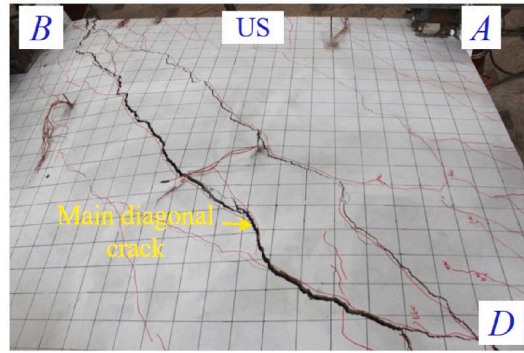
2.3.4. Discussion

Based on the above analyses, it can be summarized that with the help of GFRP materials, the NSM method is effective in strengthening the collapse resistance of beam-slab assemblages after the failure of a corner column. The above phenomenon can be attributed to that the NSM method could help the cracks to distribute more uniformly on the slab, and the tensile strength of GFRP bars in specimen NSM-series can be better utilized when the peak capacity was reached. In addition, specimen NSM2 with a smaller equivalent strengthening quantity attained excellent collapse performance compared with NSM1. Thus, employing ECC materials as a laminated layer of the slab can improve the integrity and ductility of the specimen.

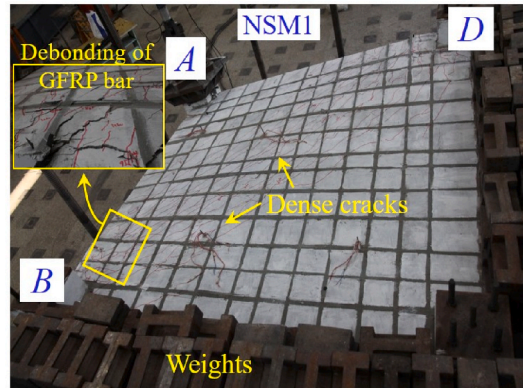
Besides, under a corner column-removal scenario, whether the beam-slab system could survive or not is mainly determined by the relationship between the peak capacity and the gravity load. Therefore, in order to theoretically evaluate the progressive collapse potential and guide for the design of the beam-slab system under accidental loads, the following sections will focus on the establishment of the theoretical method and formula for the peak capacity.

3. Mechanical analysis of frames after the failure of a corner column

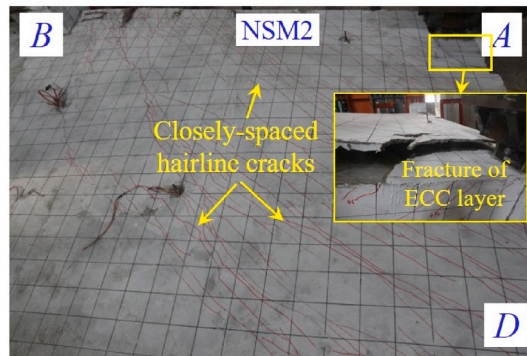
After the failure of a corner column, the progressive collapse resistance of the ALP mainly comes from the capacity of the beams and the slab; thus, the mechanical analysis of the beams and the slab must be conducted first.



(a) US



(b) NSM1



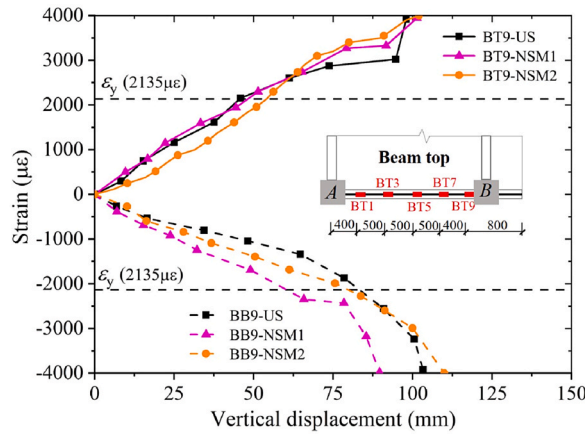
(c) NSM2

Fig. 9. Comparisons of the crack distribution of the slab for all specimens.

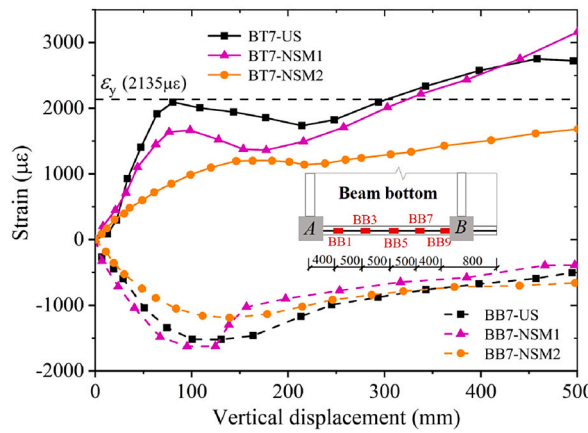
3.1. Mechanical analysis of the edge beam

After the removal of corner column A, edge beam AB and AD behave as cantilever beams, with a large bending rotation angle at end A. The deformation shape and the bending moment diagram of beam AB under uniform load are depicted in Fig. 12(a). However, the rotational constraints of the beam-column joint will limit the rotation at end A and produce positive moments. The above constraints mainly come from the bending stiffness of the upper-floor column (shown in Fig. 12(b)), the action of the slab and the torsional stiffness of beam AD (producing flexural moments M and torsional moments T , as shown in (Fig. 12(c)).

According to the above analysis, the final deformation shape and bending moment diagram of beam AB are illustrated in Fig. 12(d). After the failure of a corner column, the edge beam is subjected to combined bending, torsion and shear, and the negative bending moments at fixed end B become the control moments.



(a) BT9 and BB9



(b) BT7 and BB7

Fig. 10. Strain gauge results of edge beams.

3.2. Mechanical analysis of the slab

Fig. 13 presents the deformation shape of the slab under uniform loads before and after corner-column failure. Before the failure of a corner column, the slab region near the beams and columns is subjected to negative bending moments, while the mid-span region of the slab is under positive bending moments. However, after the corner column failed, for triangular region *ABD* of the slab, the top surface is in tension, and the bottom surface is in compression. When the vertical load is applied at end *A*, the whole triangle region *ABD* will rotate around diagonal line *BD* and fail around slab yield line *BD*, as shown in Fig. 13(b), causing the mid-span slab (without top reinforcements) to be destroyed soon. Therefore, the capacity contributed by the slab alone generally cannot satisfy the demand of progressive collapse resistance of a frame.

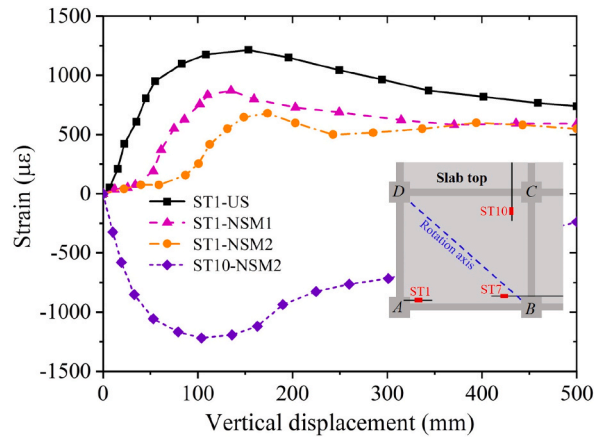
3.3. The effect of L-beam action on the flexural capacity of edge beams

The above sections separately describe the mechanical properties of the edge beam and the slab after the failure of a corner column. However, due to the integrity of the edge beam and floor slab, there exists the L-beam action. As the effective flange of the beam, the slab can enhance the flexural capacity of the beam sections, especially for the beam sections that are subjected to negative moments. Therefore, in the following sections, when calculating the progressive collapse resistance of the beam-slab system, the L-beam action should be taken into consideration.

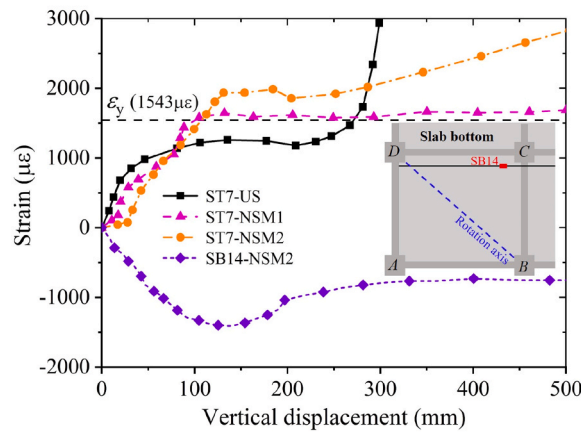
4. Theoretical method for the peak capacity of the beam-slab system

4.1. Mechanical assumption for the edge beam

According to the experimental results, the loading point is equipped with a rotational device (Fig. 4(b)). Therefore, when loading end *A* of the beam has a vertical displacement, the rotation at point *A* cannot be ignored, and the bending moments (or torsional moments) of beam *AB* are coupled with the torsional moments (or bending moments) of beam *AD*. Hence, the torsional deformation of



(a) ST1 and ST10



(b) ST7 and SB14

Fig. 11. Strain gauge results of slabs.

the beams should not be ignored.

At a large deformation, the deflection of both the edge beam and the slab inevitably produces horizontal displacement at point A, which causes out-of-plane bending moments and axial force in the edge beam. To show the existence of the axial force, the experimental results of strain gauges in edge beam AB of specimen US are presented in Fig. 14. At the initial stage of loading, the beam top bars and bottom bars were subjected to tensile force and compressive force, respectively. Thus, the gauges of the top bars and bottom bars were tensile strains and compressive strains, respectively, and the strains increased with the vertical displacement (Fig. 14(a)). At the late stage of loading (Fig. 14(b)), the strains of the tensile bars still increased with the vertical displacement; among these gauges, BT7 exceeded the yield strain of 2135 µε at a displacement of approximately 300 mm. However, the strains of the compressive bars decreased with the vertical displacement. Thus, the existence of tensile force in edge beam AB at the late stage of loading can be demonstrated.

Nevertheless, the compressive bars remained in a state of compression until the end of loading (Fig. 14(b)). Therefore, it can be concluded that the catenary action did not develop evidently and that the tensile force in edge beam AB was small enough to be ignored. Similar conclusions can be also found in the experimental results of Qian and Li [17,19]. In addition, considering that the experimental peak capacities of the specimens were generally reached at a vertical displacement of only approximately 100 mm in this study, the effect of the axial tensile force in the edge beam on the peak capacities of specimens can be ignored. As a result, the edge beam is assumed to be subjected to combined bending, torsion and shear.

4.1.1. Shear-torsion correlation

For a beam subjected to combined torsions, the shear-torsion correlation that can be appropriately expressed as a 1/4 circle appears [24] (Fig. 15(a)):

$$\left(\frac{V}{V_0}\right)^2 + \left(\frac{T}{T_0}\right)^2 = 1 \tag{1}$$

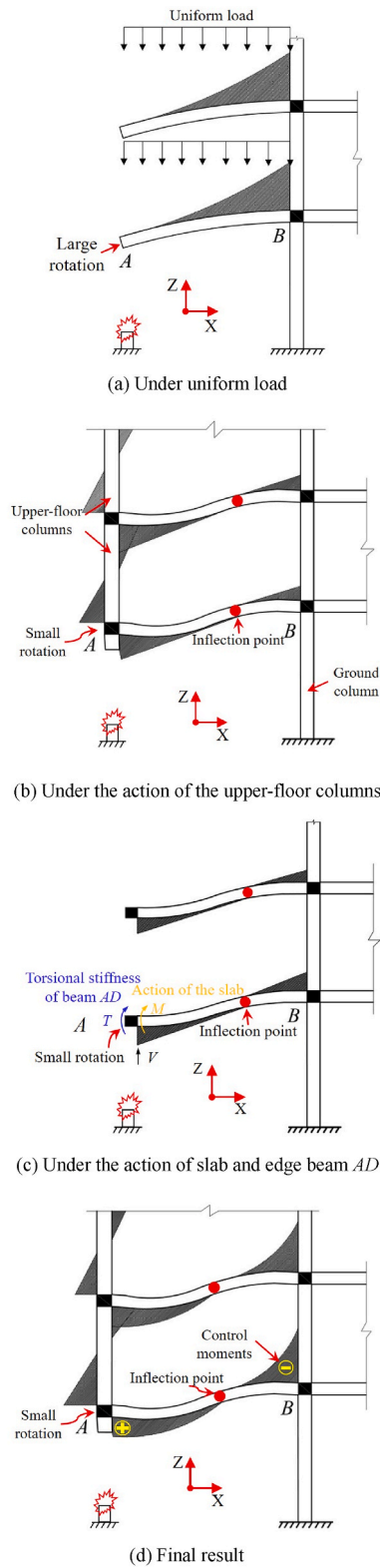
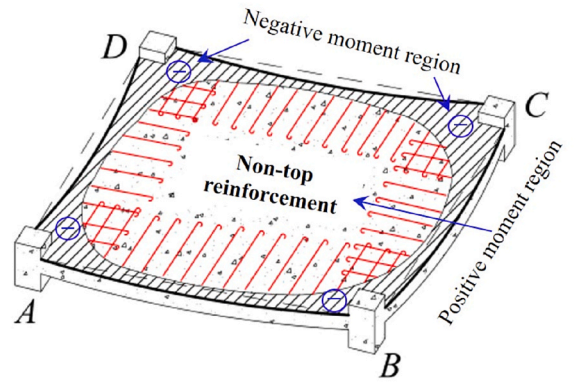
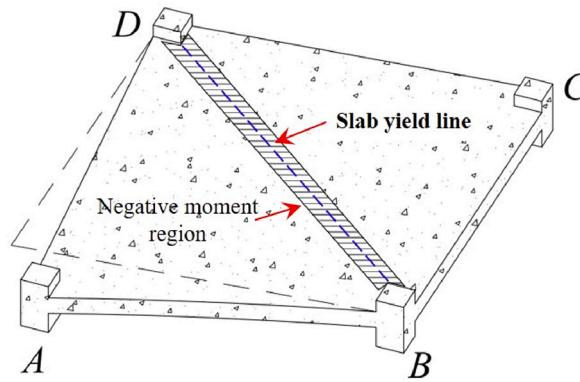


Fig. 12. The deformation shape and bending moment diagram under the corner-column failure.



(a) Before corner-column failure



(b) After corner-column failure

Fig. 13. The deformation shape and moment distribution of the slab (top view).

where V and T are the shearing capacity and torsional capacity of the beam subjected to combined shear and torsion, respectively, and V_0 and T_0 are the shearing capacity and torsional capacity of the beam subjected to pure shear and pure torsion, respectively.

For the beam under pure shear, the shearing capacity V_0 is provided by concrete bodies and shear reinforcements, which can be written as:

$$V_0 = 2\lambda\sqrt{f'_c} b_w d + \frac{A_v f_{yt} d}{s} \tag{2}$$

where f'_c is the compressive strength of the concrete; b_w is the web width of the section; d is the distance from the concrete extreme compression fiber to the centroid of longitudinal tension reinforcements; A_v is the area of shear reinforcements; f_{yt} is the yield strength of shear reinforcements within the spacing s ; s is the center-to-center spacing of shear reinforcements; λ is the modification factor and can be taken as 1.0 for ordinary concrete.

For the experimental specimens, during the loading process, the maximum shear force V on the beam is 27.15 kN, while the pure shearing capacity V_0 of the specimens is 85.60 kN in accordance with Eq. (2). According to correlation expression Eq. (1), we have $(V/V_0)^2 = 0.10$, thus $T = 0.95T_0$. The above analysis demonstrates that the shear force has little effect on the torsional capacities of specimens, so the correlation action between the shear and torsion can be ignored, and the virtual work that is done by the shear force is also ignored in the following theoretical calculations.

4.1.2. Bending-torsion correlation

According to the variable angle truss theory, the correlation curve between bending and torsion [25] is shown in Fig. 15(b) and can be expressed as:

$$\frac{M}{M_0} + r\left(\frac{T}{T_0}\right)^2 = 1 \tag{3}$$

where M is the flexural capacity of the beam subjected to combined bending and torsion; M_0 is the flexural capacity of the beam subjected to pure bending; and r is the resultant force ratio of compression reinforcements to tension reinforcements. T and T_0 are the

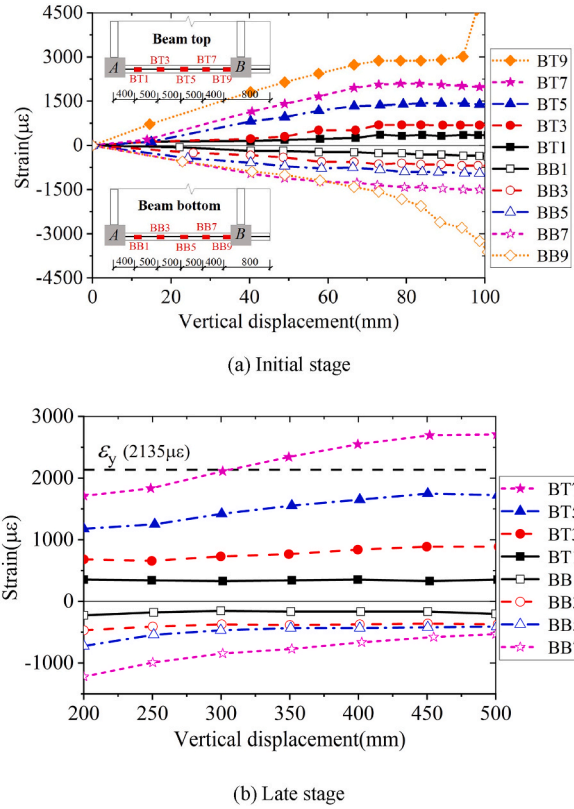


Fig. 14. Strain development of the beam longitudinal reinforcements.

same variables as those in Eq. (2).

When calculating the pure flexural capacity M_0 , the L-beam action (Fig. 16) is considered because the slab functions as the flange of the edge beam and can be expressed as:

$$\begin{cases} 0.85f'_c b_w a + f_y' A_s' = f_y A_s + f_{y1} A_{s1} \\ M_0 = 0.85f'_c b_w a (d - a/2) + f_y' A_s' (d - d') \end{cases} \quad (4)$$

where f_y and f_y' are the yield strengths of the longitudinal tension and compression reinforcements of the beam, respectively; A_s and A_s' are the cross-sectional areas of the tension and compression reinforcements of the beam, respectively; f_{y1} and A_{s1} are the yield strength and cross-sectional area of the tension reinforcements of the slab, respectively; b_f is the effective flange width, and $b_f = b_w + 6h_f$ according to ACI-318 [26], where h_f is the thickness of the slab; d' is the distance from the concrete extreme compression fiber to the centroid of the longitudinal compression reinforcements; and a is the depth of the equivalent rectangular stress block. f'_c , b_w and d are the same variables as those in Eq. (2).

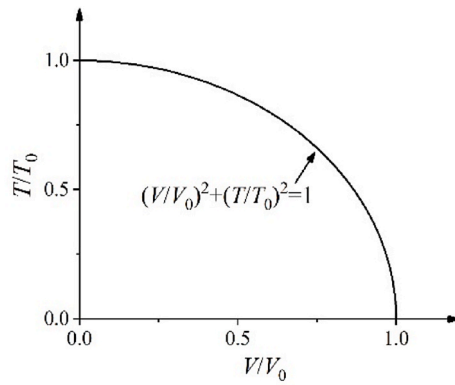
The pure torsional capacity T_0 of the L-beam section is the superposition of the torsional capacity of the rectangular section for both the web section and the effective flange section. For each rectangular section, according to the variable angle truss theory:

$$T_0 = \frac{2A_0 A_t f_{yt}}{s} \cot \theta \quad (5)$$

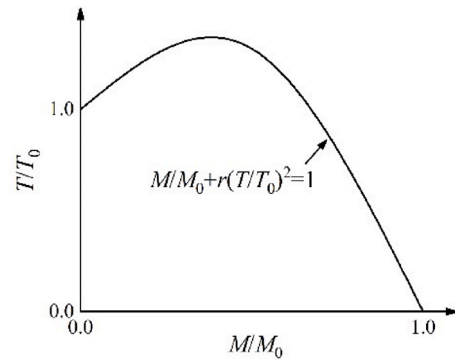
where A_0 is the area enclosed by the torsional shear flow path; A_t is the area of one leg of a closed stirrup; θ is the angle between the axis of the compression diagonal and the longitudinal axis, and $0.5 \leq \cot \theta = \sqrt{A_{st} f_y s / A_t f_{yt} u_{cor}} \leq 2.0$ [27]; A_{st} is the total area of longitudinal reinforcement to resist torsion; u_{cor} is the perimeter of the centerline of corner longitudinal torsional reinforcement; and f_y , f_{yt} and S are the same variables as those in Eq. (2).

4.1.3. Ratio of the bending moments to the torsional moments

To calculate the flexural capacity M and torsional capacity T of edge beams according to Eq. (3), the ratio of bending moments to torsional moments at fixed end sections of edge beams must be obtained first. The analytical model is shown in Fig. 17. The principle of the force method is employed to calculate the bending moments and the torsional moments of the beam section, with the vertical load P at end A. The equations can be written as:



(a) Shear-torsion correlation curve



(b) Bending-torsion correlation curve

Fig. 15. Correlation curves of the structural capacity under combined bending, shear and torsion.

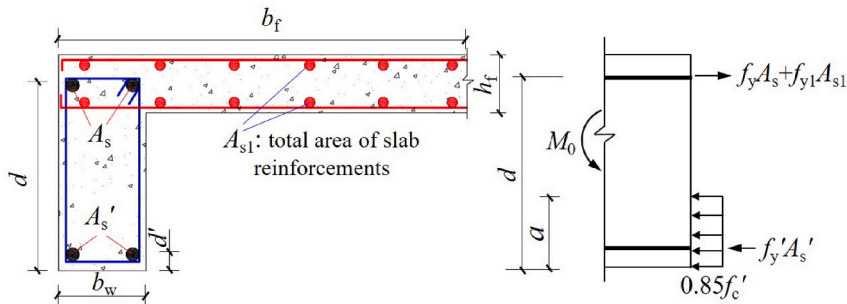


Fig. 16. Mechanical diagram of the edge beam under bending.

$$\begin{cases} \delta_{11}X_1 + \delta_{12}X_2 + \Delta_{1p} = 0 \\ \delta_{21}X_1 + \delta_{22}X_2 + \Delta_{2p} = 0 \end{cases} \tag{6}$$

where X_1 and X_2 are the torsional and bending moments of the L-beam section at end D , respectively; δ_{11} , δ_{12} , δ_{21} and δ_{22} are graphical multiplication coefficients and can be calculated according to Fig. 18; and Δ_{1p} and Δ_{2p} are the torsional angle and bending angle of the section at end D when the load P is applied at end A , respectively.

According to Eq. (6), the calculated results of X_1 and X_2 are:

$$\begin{cases} X_1 = \frac{kPl_T^2}{4(kl_T + l_L)} \\ X_2 = \frac{(kl_L^2 + 2l_T^2)P}{4(kl_L + l_T)} \end{cases} \tag{7}$$

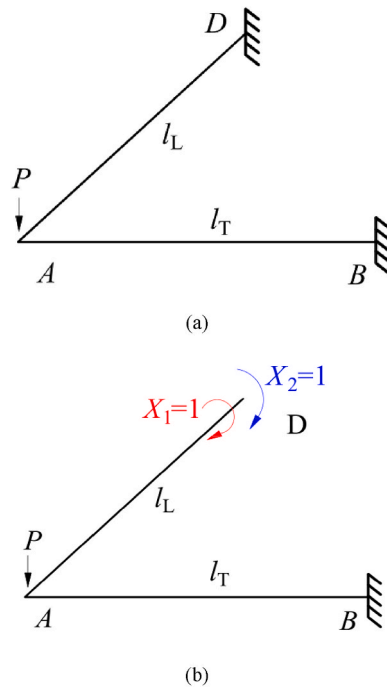


Fig. 17. Calculation diagram of force method.

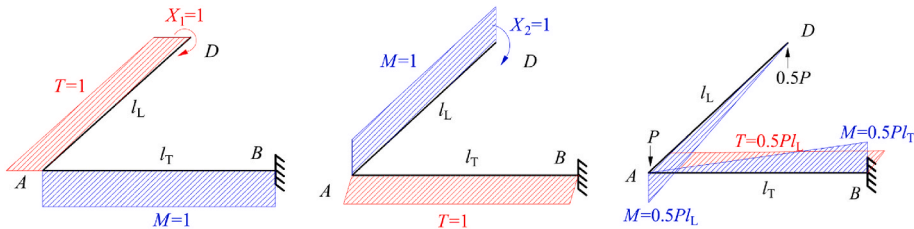


Fig. 18. Diagram of bending moments and torsional moments.

where $k = GJ/EI$; GJ and EI are the torsional stiffness and the flexural stiffness of the L-beam section, respectively; l_T and l_L are the clear spans of edge beams AB and AD , respectively; G and E are the shear modulus and elastic modulus of the L-beam section, respectively, where $G = E/(2(1 + \nu))$; ν is the Poisson's ratio of the concrete, which is taken as 0.2 in this paper; J is the torsional moment of inertia of the section about the centroidal axis, and $J = 0.6222b_w^4 + 0.3333h_f^3(b_f - b_w)$ [27]; I is the flexural moment of inertia of the section about the centroidal axis, and $I = b_w h^3/12 + (b_f - b_w)h_f^3/12 + b_w h(h/2 - y_1)^2 + h_f(b_f - b_w)(h_f/2 - y_1)^2$, where h is the depth of the edge beam and y_1 is the distance from the centroidal axis of the section to the slab top. Thus, $k = 0.182$. In this study, we also have $l_T = l_L$, so Eq. (7) becomes:

$$\begin{cases} X_1 = 0.0385Pl_T \\ X_2 = 0.4615Pl_T \end{cases} \tag{8}$$

Then, we get $X_2/X_1 \approx 12$. Therefore, the ratio of bending moments to torsional moments of the L-beam section at end D is 12. Due to the same section dimensions and beam reinforcement details, the value of the ratio is also 12 for the beam section at end B .

4.2. Formula for the peak capacity based on the principle of virtual work

After obtaining the bending moments and the torsional moments at fixed end sections of edge beams, the principle of virtual work is employed to calculate the peak capacities of specimens. When the peak capacity is attained, the following assumptions should be satisfied:

- (1). For the edge beams, the top reinforcements yield in tension, and the plastic hinge forms at the fixed end section. For the slab, the yield line forms along the diagonal line. Thus, only the virtual work done by the plastic hinge at the beam end and the yield line of the slab is considered, ignoring the virtual work contributed by the other part. The above assumption is also adopted by

Montuori R and Muscati R [28], whose research assumes that the internal virtual work is only provided by plastic hinges at the beam ends and the base sections of ground columns.

- (2). At the fixed end section of the edge beam, the structural capacity is contributed by the virtual work done by bending moments and torsional moments, and the ratio of bending moments to torsional moments of the beam section is assumed to be 12, whose reason has been presented before.
- (3). The virtual work done by the shear force and the reduction effect of the shear-torsion correlation on the torsional capacity of the fixed end section of the edge beam are ignored, and the reason has been explained in section 4.1.1.

Therefore, the failure mode of the beam-slab system is illustrated in Fig. 19. During the loading process, triangular region *ABD* of the slab rotates along the diagonal yield line *BD* as a rigid body, and its mechanical diagram is analyzed in Fig. 20. Based on the principle of virtual work, the external work (the product of load and virtual displacement) equals to the internal work (the product of moments and virtual rotation angles), thus the equation can be expressed as:

$$M_T \theta_T + M_L \theta_L + m_s l_s \theta + T_T \theta_L + T_L \theta_T = P \cdot \Delta \tag{9}$$

where M_T and M_L are the flexural capacities of plastic hinges at end *B* and *D*, respectively; T_T and T_L are the torsional capacities of beam sections at end *B* and *D*, respectively; m_s is the bending moment per unit length of the yield line of the slab; l_s is the length of the yield line of the slab; θ_T and θ_L are the rotation angles of plastic hinges at end *B* and *D*, respectively; θ is the rotation angle of the yield line of the slab; P and Δ are the vertical load and displacement at stub *A*, respectively.

The bending moment (m_s) per unit length of the yield line *BD* of the slab can be calculated as:

$$m_s = m_x \cos^2 \alpha + m_y \sin^2 \alpha = 0.5m_x + 0.5m_y \tag{10}$$

where m_x and m_y are the components of bending moment m_s along the *x*-direction and *y*-direction (Fig. 20), respectively; α is the angle between the yield line of the slab and the longitudinal axis of the edge beam. α is taken as 45° in this paper.

In addition, the following geometric relationships can be easily found in Fig. 20:

$$\begin{cases} \theta_L = \arctan \frac{\Delta}{l_L} \approx \frac{\Delta}{l_L} \\ \theta_T = \arctan \frac{\Delta}{l_T} \approx \frac{\Delta}{l_T} \\ \theta = \arctan \frac{\Delta}{l_L l_T / \sqrt{l_L^2 + l_T^2}} \approx \frac{\Delta}{l_L l_T / \sqrt{l_L^2 + l_T^2}} \end{cases} \tag{11}$$

Then, Eq. (9) becomes:

$$M_T \frac{\Delta}{l_T} + M_L \frac{\Delta}{l_L} + m_s l_s \frac{\sqrt{2}\Delta}{l_T} + T_T \frac{\Delta}{l_L} + T_L \frac{\Delta}{l_T} = P \cdot \Delta \tag{12}$$

Edge beam *AB* and *AD* have the same length and dimension parameters in this paper; thus, we have $l_T = l_L$, $M_T = M_L$, $T_T = T_L$. Finally, the peak capacity of the specimen can be expressed as:

$$P = 2M_T \frac{1}{l_T} + m_s l_s \frac{\sqrt{2}}{l_T} + 2T_T \frac{1}{l_T} \tag{13}$$

4.3. Comparisons between the theoretical results and experimental results

In order to verify the accuracy of the proposed method, the experimental results in this paper and in Ref. [20] are compared to the

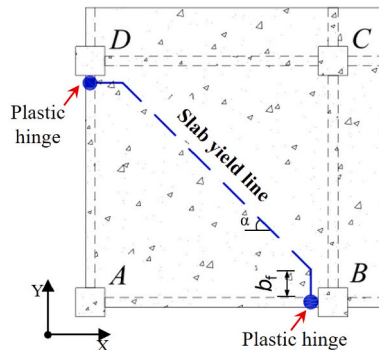


Fig. 19. Failure mode of the beam-slab system.

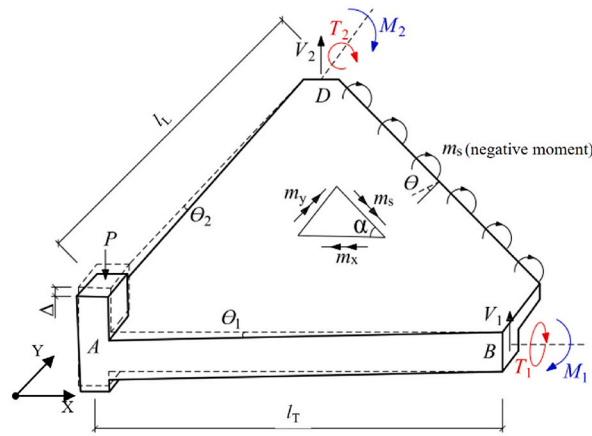


Fig. 20. Mechanical diagram of triangle slab ABD.

theoretical results by Eq. (13). The detailed calculation procedures are as follows.

4.3.1. Specimen US

When the peak capacity of the specimen is reached, for the beam section shown in Fig. 16, all the top reinforcements within the L-beam section yield in tension. The total areas of longitudinal tension and compression reinforcements of the L-beam section are $A_s + A_{s1} = 565.32 \text{ mm}^2$ ($226.19 \text{ mm}^2 + 339.12 \text{ mm}^2$) and $A_s' = 226.19 \text{ mm}^2$, respectively; thus, the ratio of r in Eq. (3) is 0.4678. According to Eqs. (4) and (5), the pure flexural capacity M_0 and pure torsional capacity T_0 of the L-beam section can be obtained. Hence, the combined flexural capacity M and torsional capacity T are calculated via Eqs. (3) and (8), as given in Table 3.

For the slab, the top reinforcements are arranged merely in the regions near the edge beams with a width of 0.625 m, leaving the top of the mid-span region nonreinforced. Thus, after excluding the top reinforcements within the L-beam section, the total length of the yield line l_s and the bending moment m_s per unit length of the yield line can be calculated by the following equations:

$$l_s = 2 \times \sqrt{2} \times 0.625 = 1.77 \text{ m}$$

$$m_s = 0.5m_x + 0.5m_y = 1.765 \text{ kN}$$

Therefore, the peak capacity of specimen US by Eq. (13) is:

$$P_{\text{theo}} = 2 \times 37.32 / 2.2 + 1.765 \times 1.77 \times \sqrt{2} / 2.2 + 2 \times 3.11 / 2.2 = 38.76 \text{ kN}$$

4.3.2. Specimen NSM-series

Specimen NSM-series is strengthened with GFRP bars embedded in the top concrete cover of the slab. For NSM1 (NSM2), the two (two) GFRP bars located within the effective flange width are assumed to contribute to the capacity of the edge beam, while the other ten (six) GFRP bars are assumed to contribute to the capacity of the slab in both the x -direction and y -direction. When specimen NSM-series reached their peak capacities, the average value of the measured strain of the GFRP bars is approximately 60% of the ultimate tensile strain; thus, the stress of 667.8 MPa is applied for calculating the capacity.

For specimen NSM1, the calculation procedures of M_0 , T_0 , M , and T are similar to those of specimen US. However, the virtual work of the yield line of the slab is done by both the top reinforcements (m_s) and the embedded GFRP bars (m_{s1}). The calculation procedure of m_s is the same as that of specimen US, and the calculation procedures of l_{s1} and m_{s1} are expressed as:

$$l_{s1} = \sqrt{2} \times 2.2 = 3.11 \text{ m}$$

$$m_{s1} = 0.5m_{x1} + 0.5m_{y1} = 4.89 \text{ kN}$$

For specimen NSM2, the slab was overlaid with a 15 mm-thick ECC layer after embedding GFRP bars. For simplicity of calculation,

Table 3 Comparisons of the peak capacity between the theoretical results and experimental results.

Specimen	M_0 (kN·m)	T_0 (kN·m)	M_T (kN·m)	T_T (kN·m)	Theoretical results P_{theo} (kN)	Experimental results P_{exp} (kN)	$P_{\text{theo}}/P_{\text{exp}}$
US	40.10	8.03	37.32	3.11	38.76	43.50	0.89
NSM1	46.20	8.03	42.12	3.51	53.27	54.30	0.98
NSM2	46.03	8.03	41.88	3.49	49.57	53.00	0.94
EBR1	45.10	8.03	41.16	3.43	50.00	48.20	1.04
EBR2	41.80	8.03	38.64	3.22	42.96	40.20	1.07

the effect of ECC layer on the capacity of edge beams is ignored, and its contributions to the capacity of the slab (m_{s2}) are calculated solely as the noncomposite specimen, which is the superposition on the capacity of the slab yield line. The calculation procedures of m_s and m_{s1} are similar to those of NSM1, and the calculation procedures of l_{s2} and m_{s2} are expressed as:

$$l_{s2} = \sqrt{2} \times 2.2 = 3.11 \text{ m}$$

$$m_{s2} = 0.5m_{x2} + 0.5m_{y2} = 0.22 \text{ kN}$$

The theoretical calculation results of the peak capacity for specimen NSM-series are given in Table 3.

4.3.3. Specimen EBR-series in reference [20]

Specimen EBR-series are the two beam-slab assemblages strengthened with externally bonded GFRP laminates on the slab. In detail, for each specimen, double GFRP laminates were bonded on the slab top surface in two directions, and the nominal thickness (t) and spacing (s) of the laminates were 0.169 mm and 515 mm, respectively. But the width (b) of the laminates was 145 mm and 70 mm for specimen EBR1 and EBR2, respectively, thus the two specimens had different equivalent strengthening quantity of 2.0 and 1.0 times $f_y A_{sbt}$. For specimen EBR-series, the material properties of steel bars were the same as those of specimen US, and the material properties of GFRP laminates and the concrete can be found in paper [20]. The calculation procedures of the peak capacity for specimen EBR-series are as follows.

In the x -direction and y -direction, one strip of GFRP laminate located within the effective flange width is assumed to contribute to the capacity of the edge beam, while the other four strips of GFRP laminate are assumed to contribute to the capacity of the yield line of the slab. According to the experimentally measured results, when specimen EBR-series reached their peak capacities, the average strain of the GFRP laminates is approximately 35% of the ultimate tensile strain, respectively; thus, the stress of 568.1 MPa is applied for calculations.

For the edge beams, the calculation procedures of M_0 , T_0 , M , and T are similar to those of specimen US. For the slab, the virtual work of the yield line consists of two parts: one is contributed by top reinforcements of the slab (m_s), which is the same as that of specimen US; the other is contributed by the externally bonded GFRP laminates (m_{s1}) along the whole length (l_{s1}) of the slab diagonal line BD . Taking EBR1 as an example, the calculations of l_{s1} and m_{s1} are expressed as:

$$l_{s1} = \sqrt{2} \times 2.2 = 3.11 \text{ m}$$

$$m_{s1} = 0.5m_{x1} + 0.5m_{y1} = 3.73 \text{ kN}$$

where m_{s1} and l_{s1} are the flexural moment and the length of the yield line, respectively, while calculating the flexural capacity contributed by the externally bonded GFRP laminates. Therefore, the peak capacity of specimen EBR1 by Eq. (13) is 50.0 kN. The calculation procedures of EBR2 are similar to those of EBR1, and the theoretical results of specimen EBR-series are given in Table 3.

4.3.4. Discussion

To evaluate the progressive collapse behavior of the test specimens after the failure of the corner column, the gravity load G_N is calculated in accordance with GSA 2013 [5]. After the failure of a corner column, the gravity load G_N applied on the corner column is controlled by the load combination $\Omega_N \cdot (1.2D + 0.5L)$, where D and L are the dead load and live load, respectively, and Ω_N is the dynamic increase factor. According to the theoretical and numerical research results obtained by Yu and Tan [14], Ω_N can be approximately taken as 1.15 in this paper. Thus, we get: $G_N = 31.77$ kN.

By comparing the theoretical capacities of the test specimens listed in Table 3 with the gravity load G_N , it can be found that with the consideration of the L-beam action of the edge beams, the test specimens would not collapse under a corner-column removal scenario. It can also be concluded from the above calculated procedures that the flexural capacity of the beam section is greatly improved due to the L-beam action.

To support this statement, the authors conducted theoretical calculations of the peak capacities of the test specimens without considering the effect of the L-beam action. The calculated results are 23.28 kN, 33.05 kN, 29.60 kN, 30.74 kN, and 26.18 kN for US, NSM1, NSM2, EBR1, and EBR2, respectively, which is the superposition of the capacity of the edge beam and the slab. The results demonstrate that the specimen capacity considering the L-beam action is approximately 65% larger than that without considering such action. From the results, we can also conclude that when the effect of the L-beam action is not considered, the progressive collapse resistance for a concrete frame is likely to be insufficient.

Besides, in Table 3, both the experimental and theoretical peak capacities of NSM1 were larger than those of EBR1, which demonstrated that the NSM method achieved a higher peak capacity than the EBR method under the same equivalent strengthening quantity. The above phenomenon can be attributed to that the NSM method could help the cracks to distribute more uniformly on the one hand (as described in section 2.3.2), on the other hand the bonding performance of the NSM method was superior to that of the EBR method, thus the tensile strength of GFRP bars in specimen NSM-series can be better utilized when the peak capacity was reached.

5. Application of the method for different structural systems

To further validate the theoretical method proposed in section 4, different structural systems are introduced, and corresponding capacities of specimens are calculated according to Eq. (13).

5.1. Beam-column system

Qian and Li [17] conducted the progressive collapse experiment of seven one-third scaled beam-column subassemblages after the failure of a corner column. Due to the difference in the specimen details and constraint conditions, the following changes should be applied to Eq. (13):

- (1). For beam-column specimens without slabs, the contribution of the slab to the peak capacity is ignored in Eq. (13).
- (2). Due to the strong constraint from the loading devices, the rigid body rotation of the loading end is limited during the tests, and the measured rotation angle of the corner joint and the torsional angle of the edge beam are very small. Thus, the virtual work done by the torsional moments is removed in Eq. (13).
- (3). Because the rotation of the corner joint is constrained, the loading end of the beam section is subjected to positive bending moments. Therefore, apart from the negative moment hinge at the fixed end, a positive moment hinge is assumed to form at the loading end of the edge beam.

Based on the above description, Eq. (13) is transformed to the following expression:

$$P = M_T \frac{1}{l_T} + M_T' \frac{1}{l_T} + M_L \frac{1}{l_L} + M_L' \frac{1}{l_L} \quad (14)$$

where M_T and M_T' are the ultimate flexural capacities of the positive moment hinge and negative moment hinge for beam T , respectively; M_L and M_L' are the ultimate flexural capacities of the positive moment hinge and negative moment hinge for beam L , respectively. l_T and l_L are the clear spans for beam T and beam L , respectively. It should be noted that beam T and beam L are the transverse beam and the longitudinal beam in the experiments [16,17,19], respectively.

The beam sections of the above specimens are symmetrically reinforced, so we have $M_T = M_T'$ and $M_L = M_L'$. Thus, Eq. (14) can be given as:

$$P = 2M_T \frac{1}{l_T} + 2M_L \frac{1}{l_L} \quad (15)$$

The theoretical results and experimental results are listed and compared in Table 4. It can be seen from the table that the theoretical results coincide with the experimental results.

5.2. Flat-slab system

Strengthening and retrofitting experiments of RC flat slabs using externally bonded CFRP laminates were carried out by Qian and Li [19] after the failure of a corner column. The performance of specimens SO-series (orthogonally bonded with CFRP laminates on the slab top) and specimens SD-series (diagonally bonded with CFRP laminates on the slab top) was compared with that of specimens Con-series (without strengthening). In the experiments, the number of CFRP laminates for strengthening is relatively large; thus, the measured maximum stress of the CFRP laminates reaches only 35% of the ultimate tensile strength. In addition, considering the uneven stress state between the CFRP laminates, the average stress is assumed to be half of the measured maximum stress for calculations.

For the flat-slab system, the virtual work done by the plastic hinges of edge beams is ignored in Eq. (13). Thus, the peak capacity of the specimen is solely provided by the yield line of the slab, which consists of the contribution of both the top reinforcements (m_s) of the slab and the CFRP laminates (m_{s1}) mounted on the slab surface. The theoretical results and experimental results of all specimens are given in Table 5, and good agreements are found.

However, the experimental results [19] demonstrated that the capacities of the SD-series specimens (diagonal strengthening) were slightly larger than those of the SO-series specimens (orthogonal strengthening). But the effect of different strengthening directions on the capacities of specimens is not reflected in Eq. (13); thus, the calculated results of the SD-series and SO-series specimens are almost the same (the slight difference shown in Table 5 arises from the different compressive strengths of the specimen concrete).

5.3. Beam-slab system with the loading end constrained

The effects of slabs on the response of RC subassemblages after the loss of a corner column were also reported by Qian and Li [16]. In their study, specimens F-series (without slabs) and S-series (with slabs) were tested under monotonic loading. Comparisons of the performance of these two series of specimens highlighted the significant contribution of slabs to the capacities of specimens.

Similar to the experiments introduced in section 5.1, the rotation at the loading end is constrained, and the virtual work done by the

Table 4
Comparisons of the peak capacity between the theoretical results and experimental results for the beam-column system.

Specimen	M_T (kN-m)	M_L (kN-m)	Theoretical results P_{theo} (kN)	Experimental results P_{exp} (kN)	P_{theo}/P_{exp}
F1	12.84	12.84	23.61	23.70	0.99
F2	18.64	18.64	34.28	36.50	0.94
F3	12.86	12.86	23.65	25.80	0.92
F4	12.88	12.88	23.70	27.50	0.86
F5	18.33	18.33	26.42	26.80	0.98
F6	12.90	18.32	25.06	26.00	0.96
F7	12.92	15.63	23.14	23.00	1.01

Table 5
Comparisons of the peak capacity between the theoretical results and experimental results for the flat-slab system.

Specimen	m_s (kN)	l_s (m)	m_{s1} (kN)	l_{s1} (m)	Theoretical results P_{theo} (kN)	Experimental results P_{exp} (kN)	P_{theo}/P_{exp}
Con-L	5.70	1.85	/	/	6.86	8.5	0.81
Con-M	11.52	1.85	/	/	13.86	14.3	0.97
SO-L	5.75	1.85	4.10	3.08	15.13	16.8	0.90
SO-M	11.76	1.85	4.10	3.08	22.35	21.3	1.05
SD-L	5.74	1.85	4.10	3.08	15.12	18.0	0.84
SD-M	11.74	1.85	4.10	3.08	22.33	22.5	0.99

torsional moments is removed in Eq. (13). At the same time, both the positive and negative plastic hinges form at the loading end section and the fixed end section of the edge beam, respectively.

However, different from the beam-column system described in section 5.1, due to the effect of the L-beam action, the flexural capacity of the negative moment hinge at the fixed end is larger than that of the positive moment hinge at the loading end. The reason was that the steel bars in the slabs are located at the tensile flange of the L-beam section for the negative moment hinge at the fixed end, while the steel bars in the slabs are located at the compressive flange of the L-beam section for the positive moment hinge at the loading end. The calculation equation of the peak capacity can be expressed as:

$$\begin{aligned}
 P &= (M_T + M_T') \frac{1}{l_T} + (M_L + M_L') \frac{1}{l_L} + m_s l_s \frac{\sqrt{l_T^2 + l_L^2}}{l_T l_L} \\
 &= \frac{2(M_T + M_T')}{l_T} + m_s l_s \frac{\sqrt{2}}{l_T} \quad (\text{if } l_T = l_L)
 \end{aligned} \quad (16)$$

where M_T and M_T' , M_L and M_L' , l_T and l_L are the same variables as those in Eq. (14); m_s and l_s are the same variables as those in Eq. (13).

The theoretical results and experimental results are listed and compared in Table 6. It can be seen from the table that the theoretical results agree well with the experimental results.

Also in Table 6, specimens S-series (with slabs) have a greatly larger capacity than specimens F-series (without slabs). Regarding the specimens with the same reinforcement details and dimensions of edge beams, due to the effect of slabs, the experimental and theoretical bearing capacities are increased by an average of 52% and 63%, respectively. Therefore, the calculation formulas derived in this paper can theoretically quantify the effect of the slab on the improvement of structural capacity, as has been described in section 4.3.4 (65% increase due to L-beam action).

6. Parametric analysis

6.1. The effect of seismic PGAs

The seismic design intensity of the prototype frame depicted in Fig. 2 is of degree 7, and the corresponding design peak ground acceleration (PGA) with a 10% probability of exceedance in 50 years is 0.10 g, in which g is the acceleration of gravity. The site classification and design earthquake classification of the frame are class III and group I, respectively. To investigate the effect of seismic PGAs of frames on the progressive collapse resistance of structural systems, this study also conducts theoretical calculations of the peak capacities of specimens whose prototype frame is designed according to other seismic PGAs, i.e., 0.05 g, 0.15 g and 0.20 g. The reinforcement ratios of edge beams of one-half scaled specimens at different seismic PGAs are given in Table 7, while the reinforcement ratios of slabs remain the same.

In addition, to compare the progressive collapse resistance between different structural systems, the flat-slab system is also designed under the same load cases as those of the above frames. The slab thickness of the prototype flat-slab structure is 200 mm and is then scaled to 100 mm according to the principle of equal reinforcement ratio. The reinforcement ratios of flat-slab specimens increase with the seismic PGAs, as shown in Table 7.

According to the reinforcement ratios of the edge beams and the flat slabs, the peak capacities of specimens calculated by Eq. (13) are obtained and listed in Table 8. In this table, for beam-column¹ specimens and beam-slab¹ specimens, the corner joint is assumed to be able to rotate, and the bending-torsion correlation is considered at the fixed end section of the edge beam; for beam-column²

Table 6
Comparisons of the peak capacities between the theoretical results and experimental results for the beam-slab system.

Specimen	M_T (kN-m)	M_T' (kN-m)	M_L (kN-m)	M_L' (kN-m)	m_s (kN)	l_s (m)	Theoretical results P_{theo} (kN)	Experimental results P_{exp} (kN)	P_{theo}/P_{exp}
F1	12.46	12.46	12.46	12.46	/	/	22.92	25.8	0.89
F2	18.64	18.64	18.64	18.64	/	/	34.28	36.5	0.94
F3	12.46	12.46	15.17	15.17	/	/	22.39	23.0	0.97
S1	12.46	25.29	12.46	25.29	5.27	1.40	39.51 (72.4%†)	39.1 (51.6%†)	1.01
S2	18.64	31.33	18.64	31.33	5.27	1.40	50.75 (48.0%†)	52.0 (42.5%†)	0.97
S3	12.46	25.29	15.17	30.68	5.27	1.40	37.64 (68.1%†)	37.5 (63.0%†)	1.01

Note: 39.51 (72.4%†) means that the theoretical peak capacity of S1 is 39.51 kN, which is 72.4% larger than capacity of F1. The above explanation law can be applied for similar expressions for specimens S1, S2 and S3 compared with F1, F2, F3, respectively.

Table 7
Reinforcement ratios of scaled specimens at different seismic PGAs (units: %).

PGA	Edge beam ($b_w \times h = 100 \text{ mm} \times 250 \text{ mm}$)			Flat-slab ($t = 100 \text{ mm}$)			
	Longitudinal bars		Transverse bars	Top		Bottom	
	Top	Bottom		Column strip	Middle strip	Column strip	Middle strip
0.05 g	0.72	0.51	0.56/0.28	0.26	0.19	0.19	0.19
0.10 g	1.15	0.83	1.01/0.50	0.33	0.26	0.26	0.26
0.15 g	1.63	1.03	1.01/0.67	0.47	0.33	0.33	0.33
0.20 g	2.07	1.61	1.01/1.01	0.72	0.46	0.46	0.46

Note: the type of longitudinal reinforcement of the edge beams is a deformed bar, while plain round bars are used as the transverse reinforcements of the edge beams and the distributed reinforcements of the slab; the material properties of the concrete and steel bars are the same as that of specimen US.

specimens and beam-slab² specimens, the rigid body rotation of the corner joint is assumed to be constrained, and flexural plastic hinges form at both ends of the edge beam accordingly.

Table 8 shows that the capacities of the specimens increase with the reinforcement ratio for each structural system, which can be mainly attributed to the improvement of the flexural capacity of the beam section. At the same seismic PGA, the capacity of the flat-slab specimen is the lowest, while the beam-slab² specimen has the maximum capacity among all the structural systems.

In addition, for every level of seismic PGA, the peak capacity of the specimen with corner joint rotation constrained is apparently larger than that of the specimen whose corner joint can rotate. This phenomenon demonstrates that the constraint stiffness from upper-floor columns plays a significant role in resisting progressive collapse under a corner column-removal scenario. For a typical concrete frame, after the failure of a corner column, the actual constraint condition of the corner joint is between the free rigid body rotation and completely constrained. Thus, the calculation results of Eq. (13) are conservative while that of Eq. (16) are unsafe. As the lower limit of the peak capacity, the results of Eq. (13) tend to be safe.

To further discuss the applicability of Eq. (13) and Eq. (16), the mechanical analysis of the typical frame after the failure of a corner column is shown in Fig. 21. The figure shows that the stiffness of the surrounding elements of the removed column, especially the upper-floor columns, has a relatively strong constraint effect on the corner joint.

In addition, at seismic PGAs of 0.05 g and 0.10 g, the capacity of the beam-slab specimen is larger than that of the beam-column specimen, which emphasizes the beneficial effect of the L-beam action on the structural capacity. However, at seismic PGAs of 0.15 g and 0.20 g, the capacity of the beam-column² specimen is larger than that of the beam-slab¹ specimen. For a beam-column² specimen, two plastic hinges form at each end of an edge beam, though L-beam action works does not exist. However, for a beam-slab¹ specimen, only one plastic hinge forms at the fixed end of an edge beam, though L-beam action exists. Therefore, the above phenomenon confirms that with the increase of the beam reinforcement ratio, two plastic hinges for one edge beam of the beam-column² specimen work more efficiently in enhancing the structural progressive collapse resistance than the L-beam action with only one plastic hinge for the beam-slab¹ specimen.

In Table 8, the peak capacities of the specimens are also compared with the gravity load $G_N = 31.77 \text{ kN}$ to estimate whether the specimens would collapse after the failure of a corner column. According to the comparison results between the theoretical capacity and the gravity load G_N , the specimens in Table 8 are divided into two groups, namely, the vulnerable collapse zone (above the red line) and the noncollapse zone (below the red line). The specimens located in the noncollapse zone would not collapse after the failure

Table 8
Peak capacity of specimens at different seismic PGAs (units: kN).

Structural system	0.05 g	0.10 g	0.15 g	0.20 g	Specimen description
Flat-slab	8.25	10.7	15.02	22.61	
Beam-column ¹	12.20	17.99	27.54	32.85	
Beam-column ²	20.80	31.29	44.33	59.05	
Beam-slab ¹	27.18	32.97	41.48	47.04	
Beam-slab ²	35.16	45.70	57.62	72.53	

Note: For beam-column¹ specimens and beam-slab¹ specimens, the corner joint can rotate with the rotation and twist of the edge beams. Therefore, Eq. (13) is utilized for beam-slab¹, and the simplified Eq. (13) without the contribution of the slab is utilized for beam column¹. For the beam-column² and beam-slab² specimens, the rotation of the corner joint is assumed to be constrained. Thus, Eq. (16) is utilized for beam-slab², and the simplified Eq. (16) without the contribution of the slab is utilized for beam-column².

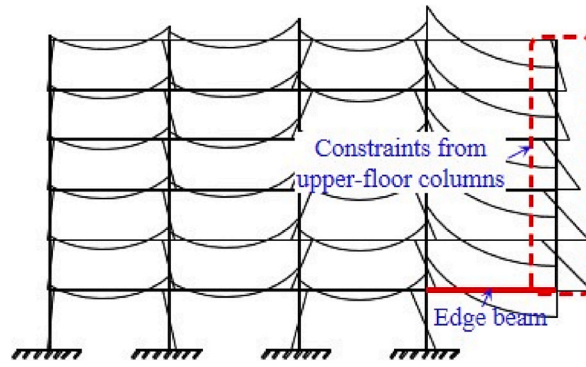


Fig. 21. Constraint action of upper-floor columns on the corner joint.

of a corner column, while the other specimens were vulnerable to progressive collapse due to insufficient capacity.

At every level of seismic PGA, the peak capacities of flat-slab specimens are lower than the gravity load G_N , leaving the disadvantage of low capacity for flat-slab systems exposed to the designers. However, for the beam-column¹ specimen (at 0.20 g), the beam-column² specimens (at 0.15 g and 0.20 g) can survive if a corner column is suddenly removed. Hence, we can see that the improvement of the beam reinforcement ratio, the constraint of the corner joint and the arrangement of the slab can reduce the risks of progressive collapse for frame structures.

6.2. The effect of over-strength factors

According to GSA 2013 [5], the design material strengths may be increased by an over-strength factor to determine the expected material strength. The over-strength factor is the ratio of the expected strength to the lower bound strength. The expected strength of a component is the statistical mean value of yield strengths for a population of similar components, and it considers the variability in material strengths as well as strain hardening and plastic section development. Thus, materials with a high strain-hardening factor and plastic development ability are beneficial to reduce the possibility of the progressive collapse of buildings.

For RC structures, the factor for concrete compressive strength is 1.5, while for steel, it is 1.25. After considering the over-strength factors of the materials, the peak capacities of the specimens mentioned in section 6.1 at different seismic PGAs are given in Table 9.

By comparing the calculated results of specimens between Tables 8 and 9, we can learn that the peak capacities of all specimens are enhanced after taking into account the over-strength factors. Compared with Table 8, the peak capacities of the three specimens in Tables 9 and i.e., the beam-column¹ specimen at 0.15 g, beam-column² specimen at 0.10 g and beam-slab¹ specimen at 0.05 g, are enhanced, the evaluation results of these three specimens have been changed and they can survive from collapse due to the over-strength factors after the failure of a corner column.

However, the improved capacities of all flat-slab specimens (32.5%–89.4% of G_N) are still lower than the gravity load G_N , so progressive collapse is inevitable for these specimens after the failure of a corner column. The progressive collapse failure of Ronan Point Apartments, whose main structural idea is the precast panels that are joined together without a structural frame [29], indicates that inadequate structural integrity and the lack of ALPs to redistribute loads are the main causes of the accident. Thus, more attention should be given to flat slabs, especially precast panels, during the evaluation of structures to mitigate progressive collapse.

6.3. The effect of frame column spacing and depth-to-span ratio

The theoretical calculations conducted in the above sections mainly investigate the progressive collapse behavior of test specimens, while the parametric analyses in this section aim at the prototype frame, which is more representative of the actual design conditions.

To investigate the effect of frame column spacing and depth-to-span ratio of beams on the peak capacity of the frames after the

Table 9
Peak capacity after considering over-strength factors (units: kN).

Structural system	0.05 g	0.10 g	0.15 g	0.20 g	Specimen description
Flat-slab	10.32	13.37	18.91	28.4	← Vulnerable collapse zone
Beam-column ¹	15.25	22.45	34.39	41.01	← Boundary line
Beam-column ²	26.00	39.12	55.41	73.81	
Beam-slab ¹	33.72	38.63	52.51	59.37	← Noncollapse zone
Beam-slab ²	44.37	57.51	72.84	91.41	

failure of a corner column, frames with different column spacings (4000 mm, 5000 mm, 6000 mm, 7000 mm, 8000 mm) and different depth-to-span ratios (1/12, 1/11, 1/10, 1/9, 1/8) are designed according to the seismic PGA of 0.10 g, while the depth-to-width ratio of the beam section is kept at approximately 2.5. In addition, the frame in two directions of the plan view has the same column spacing, section dimensions and reinforcement details. The section dimensions and the reinforcement ratios of the beams are listed in Table 10. For convenience of calculations, the thickness of the slab and the bending moment per unit length of the yield line of the slab are taken to be 140 mm and 12.3 kN for all the frames, respectively.

When calculating the peak capacity of the above frames, it is assumed that the rotation of the corner joint is constrained by the upper-floor columns and other surrounding members, and plastic hinges form at both end sections of the edge beams. Thus, while considering the L-beam action, Eq. (16) is adopted for the theoretical calculations. In addition, the gravity load G_N is also calculated to estimate whether the frames would collapse after the failure of a corner column. The comparisons between the peak capacities of the frames and the gravity load G_N are illustrated in Fig. 22.

As shown in Fig. 22(a), we can learn that under the same column spacing, the peak capacities of the frames increase with the depth-to-span ratio. In addition, when the depth-to-span ratio remains unchanged, the larger the column spacing is, the more evidently the peak capacity of the frame increases. The above phenomenon can be attributed to the improved flexural capacity of the beam section. A sharp increase of peak capacity can be found for the frames when the column spacing changes from 5000 mm to 6000 mm due to the flexural capacities of secondary beams, as presented in Fig. 22(b).

However, the demand of the gravity load does not increase much with the depth-to-span ratio; hence, the greater the depth-to-span ratio is, the larger the safety margin of the frame. But when the column spacing increases, the demand of the gravity load increases sharply, so the safety margin of the frame decreases with the column spacing. By comparing the peak capacities of the frames with the demand gravity load, it can be concluded that all the frames will not collapse after the failure of a corner column except for the three frames with a column spacing of 8000 mm (enclosed by the red line in Table 10).

To prevent the above frames from progressive collapse, the seismic PGA of frames is improved to 0.15 g, and the corresponding reinforcement ratios are given in Table 11. The comparisons between the peak capacities of the frames and the demand gravity load are shown in Fig. 23. It can be seen from the figure that all the frames would not collapse after the failure of a corner column according to the seismic PGA of 0.15 g, and the conclusion is reached that increasing the seismic PGA of a frame is beneficial to preventing progressive collapse.

6.4. The effect of top full-length reinforcements in the slab

In some residential design specifications of China, the floor slabs are required to be arranged full-length top reinforcements along both directions within the two end bays of the residential building. For example, specification 7.1.1–4 of Standard for Quality Control of Common Failing of Housing Engineering (DGJ32/J 16) [30] stipulates that the slab at end bays shall be reinforced with full-length steel bars in both directions of the top and bottom of the slab; the diameter and the spacing of steel bars shall not be less than 8 mm and shall not be greater than 100 mm, respectively.

For the specimens in Table 3, if the top of the slab is reinforced with full-length steel bars in both directions, the peak capacity will be enhanced by at least 5.7%. Therefore, in terms of a frame building constructed according to the above regulations, the progressive collapse resistance of the frame can be slightly improved after the failure of a corner column.

Table 10
Section dimensions and reinforcement ratios of the beams according to seismic PGA of 0.10 g

Column spacing	Depth-to-span ratio				
	1/12	1/11	1/10	1/9	1/8
4000 mm	130 mm×330	140 mm×360	160 mm×400	180 mm×450	200 mm×500
	mm (1.86%, 0.84%)	mm (1.55%, 0.62%)	mm (1.19%, 0.45%)	mm (0.91%, 0.33%)	mm (0.72%, 0.25%)
5000 mm	170 mm×420	180 mm×450	200 mm×500	220 mm×550	250 mm×630
	mm (1.63%, 0.69%)	mm (1.34%, 0.54%)	mm (1.06%, 0.42%)	mm (0.83%, 0.32%)	mm (0.67%, 0.24%)
6000 mm	200 mm×500	220 mm×550	240 mm×600	260 mm×660	300 mm×750
	mm (1.48%, 0.80%)	mm (1.25%, 0.61%)	mm (0.96%, 0.45%)	mm (0.77%, 0.36%)	mm (0.58%, 0.28%)
7000 mm	230 mm×580	250 mm×630	280 mm×700	310 mm×780	350 mm×870
	mm (1.32%, 0.79%)	mm (1.07%, 0.59%)	mm (0.83%, 0.44%)	mm (0.67%, 0.35%)	mm (0.53%, 0.27%)
8000 mm	260 mm×660	290 mm×730	320 mm×800	360 mm×890	400 mm×1000
	mm (1.22%, 0.76%)	mm (0.95%, 0.58%)	mm (0.76%, 0.44%)	mm (0.60%, 0.33%)	mm (0.46%, 0.25%)

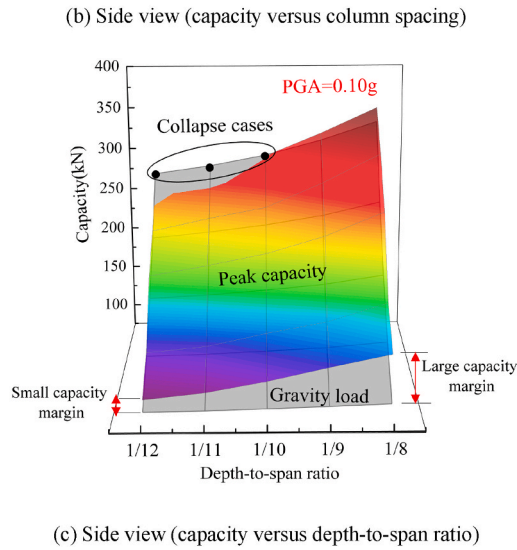
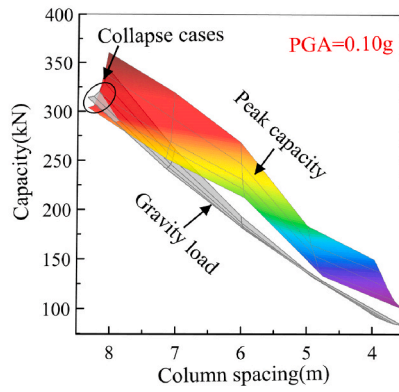
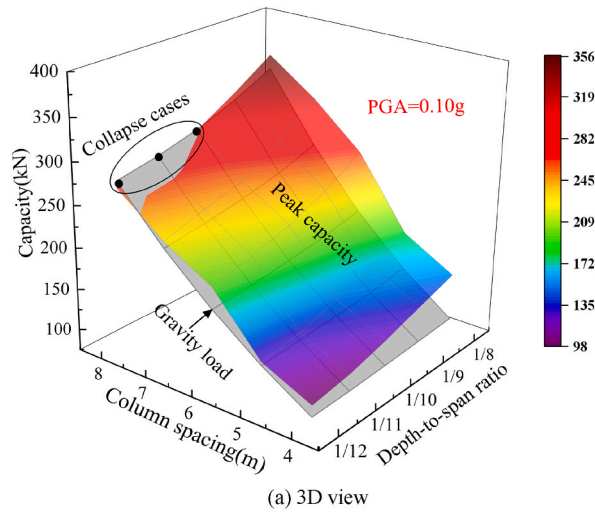


Fig. 22. Comparisons between the peak capacities of the frames and the gravity load at a seismic PGA of 0.10 g.

6.5. The importance of the integrity of beams and slabs

Compared with cast-in-situ frames, an assembled frame cannot utilize the L-beam action well. If the integrity of the slabs and the beams is poor, the slabs cannot be treated as the effective flanges of the beams. Thus, the contribution of the slabs and the beams should

Table 11
Section dimensions and reinforcement ratios of the beams according to seismic PGA of 0.15 g

Column spacing	Depth-to-span ratio				
	1/12	1/11	1/10	1/9	1/8
4000 mm	130 mm × 330 mm (1.94%, 0.89%)	140 mm × 360 mm (1.57%, 0.71%)	160 mm × 400 mm (1.19%, 0.51%)	180 mm × 450 mm (0.92%, 0.37%)	200 mm × 500 mm (0.73%, 0.27%)
5000 mm	170 mm × 420 mm (1.82%, 0.76%)	180 mm × 450 mm (1.48%, 0.61%)	200 mm × 500 mm (1.11%, 0.44%)	220 mm × 550 mm (0.86%, 0.33%)	250 mm × 630 mm (0.64%, 0.24%)
6000 mm	200 mm × 500 mm (1.77%, 0.88%)	220 mm × 550 mm (1.42%, 0.71%)	240 mm × 600 mm (1.07%, 0.51%)	260 mm × 660 mm (0.83%, 0.37%)	300 mm × 750 mm (0.61%, 0.25%)
7000 mm	230 mm × 580 mm (1.71%, 0.79%)	250 mm × 630 mm (1.33%, 0.59%)	280 mm × 700 mm (1.03%, 0.45%)	310 mm × 780 mm (0.78%, 0.35%)	350 mm × 870 mm (0.57%, 0.27%)
8000 mm	260 mm × 660 mm (1.53%, 0.77%)	290 mm × 730 mm (1.21%, 0.59%)	320 mm × 800 mm (0.94%, 0.45%)	360 mm × 890 mm (0.70%, 0.34%)	400 mm × 1000 mm (0.54%, 0.26%)

Note: the section dimensions and reinforcement ratios of the secondary beams are the same as those in Table 10.

be calculated separately without considering the L-beam action. For the specimens in Table 3, if the contribution of the slabs and the beams is calculated separately without consideration of the L-beam action, the peak capacity will be reduced by approximately 40%. Due to the importance of the integrity of the slabs and the beams, the arrangement of the cast-in-situ superimposed layer of the slabs and beams (shown in Fig. 24(a)) for an assembled frame is essential to ensure the progressive collapse resistance of the frame because the cast-in-situ superimposed layer can help the slabs and beams work together. Therefore, the progressive collapse resistance of assembled monolithic frame is larger than that of the traditional pure precast frame (shown in Fig. 24(b)).

6.6. Discussion

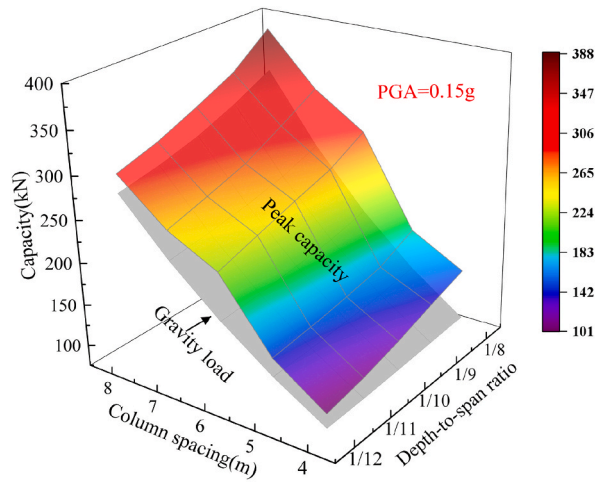
Due to the effect of the L-beam action, cast-in-situ RC slabs are efficient in enhancing the progressive collapse resistance of frame structures by improving the flexural capacity of the beam section. After the sudden removal of a corner column, if the rotation of the corner joint can be constrained, plastic hinges will form at both end sections of the edge beam, which can maximize the flexural capacity of edge beams.

Through comparisons between the capacities of specimens and the gravity load G_N in Tables 8–11, it is indicated that both amplifying the longitudinal reinforcement ratios of edge beams and employing the over-strength factors are capable of improving the performance of RC frames against progressive collapse caused by the loss of a corner column. Therefore, buildings located in regions with high earthquake intensity or buildings reinforced by reinforcements with a high over-strength factor have high capacity or high capacity margins and thus are less prone to progressive collapse failure.

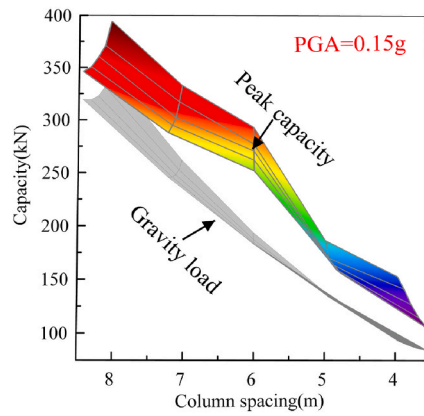
7. Conclusions

This study presents the experimental results of RC subassemblages strengthened with near-surface-mounted GFRP bars and an ECC layer (specimen NSM-series), and proposes a theoretical method to estimate the progressive collapse resistance of RC subassemblages after the failure of a corner column. The following conclusions can be drawn:

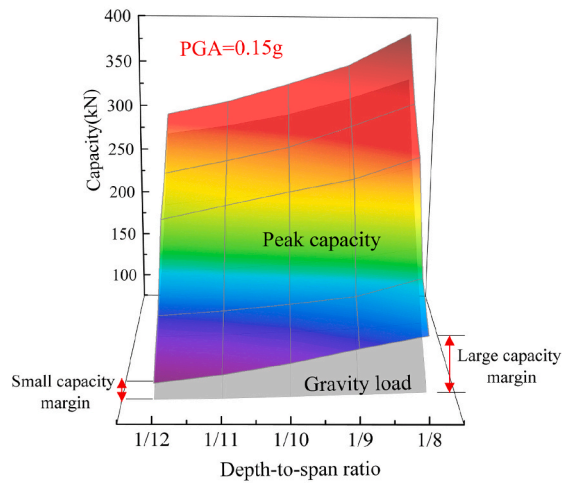
- (1) Experimental results found that the collapse resistance of beam-slab subassemblages was effected by strengthening methods and the equivalent strengthening quantity of GFRP materials, and the NSM method achieved a higher peak capacity than the EBR method under the same equivalent strengthening quantity. Compared with the control specimen US, no main crack but dense and small cracks formed on the slab top of specimen NSM-series, in which the tensile strength of GFRP bars can be better utilized. The multi-cracking behavior of ECC materials helped specimen NSM2 to develop closely-spaced hairline cracks on the slab top and improved the integrity of the whole specimen.
- (2) According to the experimental results, after the failure of a corner column, the edge beam in a frame structure was subjected to a combined tensile force, bending moment, shear force, and torsional moment. However, experimental results and theoretical analyses demonstrated that the effect of axial force and shear force on the edge beam was small enough to be ignored while calculating the peak capacity. Based on the principle of virtual work and yield-line theory, a theoretical calculation method of the peak capacity of an RC beam-slab structural system after losing a corner column was proposed. The above method is also suitable for other structural systems: the beam-column system and the flat-slab system.
- (3) On the basis of the theoretical formula, the contribution of the slabs to the structural capacity was quantitatively evaluated. Due to the effect of the L-beam action, the capacities of beam-slab specimens can be enhanced by 52%–65% compared with that without considering such action. Due to the L-beam action, the strengthening schemes aimed at the slabs can evidently enhance the capacities of beam-slab systems.
- (4) Parametric analyses indicate that the capacity of the flat-slab system is the lowest when compared with that of the beam-column system and beam-slab system after the failure of a corner column. The flat-slab system has a high vulnerability to progressive collapse because no beams could assist in redistributing the axial load previously carried by the failed columns. Even after considering the over-strength factors of the materials, the peak capacities (32.5%–89.4% of G_N) are still lower than the demand of gravity load G_N .



(a) 3D view



(b) Side view (capacity versus column spacing)



(c) Side view (capacity versus depth-to-span ratio)

Fig. 23. Comparisons between the peak capacities of the frames and the gravity load at a seismic PGA of 0.15 g.

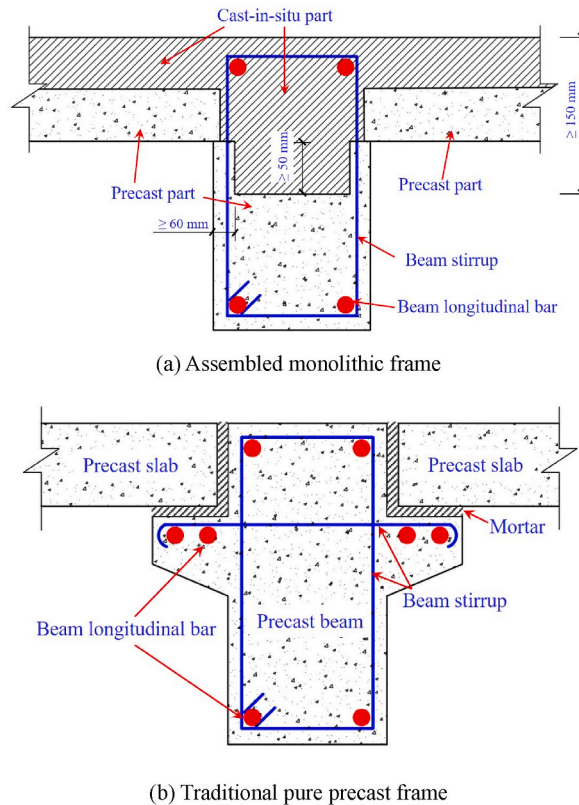


Fig. 24. Beam sections of an assembled monolithic frame and a traditional pure precast frame.

- (5) Both experimental results and theoretical analyses indicate that increasing the flexural capacity of the beam section is an effective way to improve the performance of RC frames against progressive collapse under a corner column-removal scenario, which can be achieved by increasing the reinforcement ratio of the beam, utilizing materials with a high strain-hardening factor and plastic development ability. Improving the rotational constraint stiffness of the corner joint is also a strong measure to enhance the structural capacity. In addition, if concrete slabs are configured with full-length top reinforcements along both directions within the two end bays, the progressive collapse resistance of the frames can be improved by at least 5.7% for test specimens after the failure of a corner column.
- (6) The arrangement of the cast-in-situ superimposed layer in assembled monolithic frames is important to ensure the progressive collapse resistance for the purpose of fully utilizing the L-beam action. The peak capacity will be reduced by approximately 40% if the cast-in-situ superimposed layer is not arranged for the assembled frames, where the L-beam action cannot be considered, taking the test specimens in this study as examples.

CRedit authorship contribution statement

Weihong Qin: Conceptualization, Methodology, Resources, Funding acquisition, Supervision. **Zhuo Xi:** Conceptualization, Supervision. **Xinyu Liu:** Methodology, Investigation, Data curation, Writing – original draft. **Peng Feng:** Investigation, Data curation. **Xin Ou:** Validation. **Jianxiang Yang:** Validation.

Declaration of competing interest

The authors declare that they have no known competing financial interests or personal relationships that could have appeared to influence the work reported in this paper.

Acknowledgments

This research was supported by the National Key Research and Development Program of China (No. 2017YFC0703000) and the National Natural Science Foundation of China (Nos. 51778330 and 51522807). The opinions, findings and conclusions expressed in this paper are those of the authors and do not necessarily be interpreted as those of the supporting institution.

Appendix A. Supplementary data

Supplementary data to this article can be found online at <https://doi.org/10.1016/j.job.2021.103805>.

References

- [1] British Standard Institute (BSI), *Structural Use of Concrete, Part 1: Code of Practice for Design and Construction*, 1997. London.
- [2] European Committee for Standardization (CEN), *Eurocode 1: Actions on Structures, Part 1–7, General actions—Accidental actions*, Belgium, 2006.
- [3] ASCE 7–10, *Minimum Design Loads for Buildings and Other Structures*, 2010. Reston, vol. A.
- [4] Department of Defense (DoD), *Design of Structures to Resist Progressive Collapse*, 2009. Washington, DC.
- [5] General Services Administration (GSA), *Progressive Collapse Analysis and Design Guidelines for New Federal Office Buildings and Major Modernization Projects*, 2013. Washington, DC.
- [6] J. Yu, K.H. Tan, Experimental and numerical investigation on progressive collapse resistance of reinforced concrete beam column sub-assemblages, *Eng. Struct.* 55 (4) (2013) 90–106, <https://doi.org/10.1016/j.engstruct.2011.08.040>.
- [7] J. Yu, K.H. Tan, Structural behavior of RC beam-column subassemblages under a middle column removal scenario, *J. Struct. Eng.* 139 (2) (2013) 233–250, [https://doi.org/10.1061/\(ASCE\)ST.1943-541X.0000658](https://doi.org/10.1061/(ASCE)ST.1943-541X.0000658).
- [8] Y.H. Bao, H.S. Lew, S.K. Kunnath, Modeling of reinforced concrete assemblies under column-removal scenario, *J. Struct. Eng.* 140 (1) (2014), 04013026, [https://doi.org/10.1061/\(ASCE\)ST.1943-541X.0000773](https://doi.org/10.1061/(ASCE)ST.1943-541X.0000773).
- [9] A.T. Pham, K.H. Tan, J. Yu, Numerical investigations on static and dynamic responses of reinforced concrete sub-assemblages under progressive collapse, *Eng. Struct.* 149 (15) (2016) 2–20, <https://doi.org/10.1016/j.engstruct.2016.07.042>.
- [10] K. Qian, B. Li, J.X. Ma, Load-carrying mechanism to resist progressive collapse of RC buildings, *J. Struct. Eng.* 141 (2) (2014), 4014107, [https://doi.org/10.1061/\(ASCE\)ST.1943-541X.0001046](https://doi.org/10.1061/(ASCE)ST.1943-541X.0001046).
- [11] X.Z. Lu, K.Q. Lin, Y. Li, et al., Experimental investigation of RC beam-slab substructures against progressive collapse subject to an edge-column-removal scenario, *Eng. Struct.* 149 (2017) 91–103, <https://doi.org/10.1016/j.engstruct.2016.07.039>.
- [12] X.J. Yang, F. Lin, X.L. Gu, Experimental study on a novel method to improve progressive collapse resistance of RC frames using locally debonded rebars, *J. Build. Eng.* 41 (2021) 102428, <https://doi.org/10.1016/j.job.2021.102428>.
- [13] Y.P. Su, Y. Tian, X.S. Song, Progressive collapse resistance of axially-restrained frame beams, *ACI Struct. J.* 106 (5) (2009) 600–607.
- [14] J. Yu, K.H. Tan, Analytical model for the capacity of compressive arch action of reinforced concrete sub-assemblages, *Mag. Concr. Res.* 66 (3) (2014) 109–126, <https://doi.org/10.1680/mac.13.00217>.
- [15] J. Hou, Z. Yang, Simplified models of progressive collapse response and progressive collapse-resisting capacity curve of RC beam-column substructures, *J. Perform. Constr. Facil.* 28 (4) (2014), 4014008, [https://doi.org/10.1061/\(ASCE\)CF.1943-5509.0000492](https://doi.org/10.1061/(ASCE)CF.1943-5509.0000492).
- [16] K. Qian, B. Li, Slab effects on response of reinforced concrete substructures after loss of corner column, *ACI Struct. J.* 109 (6) (2012) 845–855.
- [17] K. Qian, B. Li, Performance of three-dimensional reinforced concrete beam-column substructures under loss of a corner column scenario, *J. Struct. Eng.* 139 (4) (2013) 584–594, [https://doi.org/10.1061/\(ASCE\)ST.1943-541X.0000630](https://doi.org/10.1061/(ASCE)ST.1943-541X.0000630).
- [18] K. Qian, B. Li, Quantification of slab influences on the dynamic performance of RC frames against progressive collapse, *J. Perform. Constr. Facil.* 29 (1) (2013), 04014029, [https://doi.org/10.1061/\(ASCE\)CF.1943-5509.0000488](https://doi.org/10.1061/(ASCE)CF.1943-5509.0000488).
- [19] K. Qian, B. Li, Strengthening and retrofitting of RC flat slabs to mitigate progressive collapse by externally bonded CFRP laminates, *J. Compos. Construct.* 17 (4) (2013) 554–565, [https://doi.org/10.1061/\(ASCE\)CC.1943-5614.0000352](https://doi.org/10.1061/(ASCE)CC.1943-5614.0000352).
- [20] P. Feng, H.L. Qiang, X. Ou, et al., Progressive collapse resistance of GFRP-strengthened RC beam-slab subassemblages in a corner column-removal scenario, *J. Compos. Construct.* 23 (1) (2019), 04018076, [https://doi.org/10.1061/\(ASCE\)CC.1943-5614.0000917](https://doi.org/10.1061/(ASCE)CC.1943-5614.0000917).
- [21] S.B. Kang, K.H. Tan, E.H. Yang, Progressive collapse resistance of precast beam–column sub-assemblages with engineered cementitious composites, *Eng. Struct.* 98 (2015) 186–200, <https://doi.org/10.1016/j.engstruct.2015.04.034>.
- [22] Ministry of Housing and Urban-Rural Development of the People’s Republic of China (MOHURD), *Code for Design of Concrete Structures*, GB 50010, Beijing, 2010 (in Chinese).
- [23] Ministry of Housing and Urban-Rural Development of the People’s Republic of China (MOHURD), *Code for Seismic Design of Buildings*, GB 50011, Beijing, 2010 (in Chinese).
- [24] X.F. Lian, Z.D. Wang, Z.Q. Wang, An experimental research of the behavior of rectangular reinforced concrete beams with web reinforcement under combined torsion, shear and bending, *J. HRB. Univ. C E Arch.* 1 (1985) 23–30 (in Chinese).
- [25] T.T.C. Hsu, *Torsion of Reinforced Concrete*, Van Nostrand Reinhold Company, New York, 1984.
- [26] American Concrete Institute Committee 318 (ACI-318), *Building Code Requirements for Structural Concrete and Commentary*, 2014. Farmington Hills, MI.
- [27] K.N. Rahal, M.P. Collins, Simple model for predicting torsional strength of reinforced and prestressed concrete sections, *ACI Struct. J.* 93 (6) (1996) 658–666.
- [28] R. Montuori, R. Muscati, Plastic design of seismic resistant reinforced concrete frame, *Earthq. Struct.* 8 (1) (2015) 205–224, <https://doi.org/10.12989/eas.2015.8.1.205>.
- [29] C. Pearson, N. Delatte, Ronan point apartment tower collapse and its effect on building codes, *J. Perform. Constr. Facil.* 19 (2) (2005) 172–177, [https://doi.org/10.1061/\(ASCE\)0887-3828\(2005\)19:2\(172\)](https://doi.org/10.1061/(ASCE)0887-3828(2005)19:2(172)).
- [30] Construction Department of Jiangsu Province, *Standard for Quality Control of Common Failing of Housing Engineering* (in Chinese), 2005. DGJ32/J 16, Nanjing.